

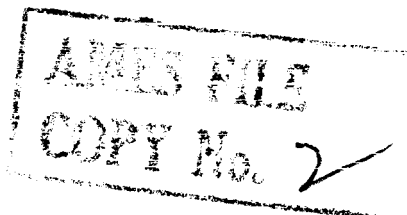
OCT 2 1961

UNCLASSIFIED  
~~CONFIDENTIAL~~

Copy

20

NASA TM X-574



# TECHNICAL MEMORANDUM

## X-574

CLASSIFICATION CHANGED TO UNCLASSIFIED  
BY AUTHORITY OF NASA CLASSIFICATION CHANGE  
NOTICES, CHANGE NO. 215-96 EFF. 10/18/71

EFFECTS OF SPIKE-MOUNTED FLOW DEFLECTORS ON THE  
TRANSONIC AERODYNAMIC CHARACTERISTICS OF A  
BLUNT-NOSED BODY OF REVOLUTION HAVING A  
CYLINDRICAL OR FLARED AFTERBODY

By Stuart L. Treon, Roy M. Wakefield,  
and Earl D. Knechtel

Ames Research Center  
Moffett Field, Calif.

CLASSIFIED DOCUMENT - TITLE UNCLASSIFIED

This material contains information affecting the national defense of the United States within the meaning of the espionage laws, Title 18, U.S.C., Secs. 793 and 794, the transmission or revelation of which in any manner to an unauthorized person is prohibited by law.

NATIONAL AERONAUTICS AND SPACE ADMINISTRATION  
WASHINGTON

October 1961

~~CONFIDENTIAL~~  
UNCLASSIFIED

87014

UNCLASSIFIED

C [REDACTED]

NATIONAL AERONAUTICS AND SPACE ADMINISTRATION

TECHNICAL MEMORANDUM X-574

EFFECTS OF SPIKE-MOUNTED FLOW DEFLECTORS ON THE  
TRANSONIC AERODYNAMIC CHARACTERISTICS OF A  
BLUNT-NOSED BODY OF REVOLUTION HAVING A  
CYLINDRICAL OR FLARED AFTERBODY\*

By Stuart L. Treon, Roy M. Wakefield,  
and Earl D. Knechtel

SUMMARY

An investigation has been conducted in a transonic wind tunnel to determine the static aerodynamic characteristics of a blunt-nosed body of revolution having a cylindrical or flared afterbody and equipped with various flow deflectors. The flow deflectors had either a flat or a hemispherical face and were affixed to the model by means of a spike projecting forward from the model nose. Data are presented for angles of attack from  $-2^{\circ}$  to  $+14^{\circ}$  at ten Mach numbers from 0.6 to 1.4. The test Reynolds number was 0.50 million based on the cylindrical body diameter.

INTRODUCTION

Demand for aerodynamic data for low-fineness-ratio bodies of revolution at transonic speeds stems not only from interest in atmosphere-entry vehicles, but also from an awareness that the stability of such bodies can vary greatly in the transonic speed range. The present report is one of a series presenting the results of an investigation conducted at the Ames Research Center to determine the effects of systematic changes in model geometry on the aerodynamic characteristics of low-fineness-ratio bodies at transonic speeds. Previous phases of the investigation are reported in references 1 through 5. In the present report are the results of an investigation of the effects of spike-mounted flow deflectors on the static aerodynamic characteristics of a blunt-nosed, low-fineness-ratio body of revolution with a cylindrical or flared afterbody. The

\*Title, Unclassified

C [REDACTED]

UNCLASSIFIED

flow deflectors were either hemispherical or flat-faced and were mounted on a spike extending from 1.5 to 2.5 model body diameters ahead of the model nose.

The results are presented without detailed discussion.

#### NOTATION

B	model base area
$C_A$	measured axial-force coefficient, $\frac{\text{measured axial force}}{qS}$
$C_{A_b}$	base axial-force coefficient, $\frac{(p_\infty - p_b)B}{qS}$
$C_{A_f}$	forebody axial-force coefficient, $C_A - C_{A_b}$
$C_m$	pitching-moment coefficient about nose-body juncture, $\frac{\text{pitching moment}}{qSd}$
$\frac{C_m}{\alpha}$	the slope of a straight line drawn from $C_m$ at $\alpha = 0^\circ$ to any point on the $C_m$ vs. $\alpha$ curve
$C_N$	normal-force coefficient, $\frac{\text{normal force}}{qS}$
$\frac{C_N}{\alpha}$	the slope of a straight line drawn from $C_N$ at $\alpha = 0^\circ$ to any point on the $C_N$ vs. $\alpha$ curve
c.p.	center-of-pressure location in body diameters, positive when forward of the moment reference shown in figure 1, $\frac{C_m/\alpha}{C_N/\alpha}$
d	cylindrical body diameter
M	Mach number
$p_b$	base pressure
$p_\infty$	test section static pressure
q	dynamic pressure
S	cross-sectional area of cylindrical centerbody

$\alpha$  angle of attack, deg

### Model Component Designations

$B_x$  cylindrical body, subscript denoting length in body diameters  
 $D_x$  flow deflector, subscript denoting shape (See fig. 1)  
 $F_{20-4}$  flared afterbody, semivertex angle =  $20^\circ$  and ratio of flare base area to cylindrical body cross-sectional area = 4  
 $L_x$  spike, subscript denoting length in cylindrical body diameters  
 $N_{10}$  nose, subscript denoting tenth nose in series (See ref. 4)

### APPARATUS AND MODELS

The investigation was conducted in the Ames 2- by 2-Foot Transonic Wind Tunnel, which is of the closed-circuit, variable-pressure type. This facility (ref. 6) has a perforated test section which permits continuous, choke-free operation from subsonic speeds up to Mach number 1.4.

The configurations investigated were various combinations of two spike-mounted flow deflectors on a blunt-nosed body of revolution with and without a flared afterbody (fig. 1). The nose was a spherical segment and was affixed to either a cylindrical body or a cylindrical body with a  $20^\circ$  flared afterbody. The flow deflectors were hemispherical or disk-shaped and the spike length was varied from 1.5 to 2.5 cylindrical body diameters. The model with the cylindrical body was tested with the hemispherical flow deflectors only, whereas the model with the flared afterbody was tested with both flow deflectors.

The models were mounted in the test section on a sting-supported strain-gage balance which was shielded by a metal shroud as shown in figure 1. The position of the shroud with respect to the model base was the same for all of the models. A photograph of a model installed in the test section is shown in figure 2.

### TESTS AND DATA REDUCTION

The investigation was conducted at Mach numbers from 0.6 to 1.4 at angles of attack from approximately  $-2^\circ$  to  $+14^\circ$ . At all test Mach



numbers, the angle of attack was decreased from an initial  $0^\circ$  to approximately  $-2^\circ$ , then increased progressively to about  $+14^\circ$ . At Mach numbers greater than 0.90, the angle of attack was decreased from  $+14^\circ$  to  $-2^\circ$  to determine the possible occurrence of flow hysteresis of the type discussed in reference 7 for blunt-nosed bodies and observed in several phases of the investigation previously reported (refs. 3, 4, and 5). The Reynolds number based on the cylindrical body diameter was 0.50 million.

In order to restrict the variation of boundary-layer transition location, boundary-layer trip wires were affixed to the cylindrical portion of the model as shown in figure 1. The effectiveness of the trip wires was determined from flow-visualization studies, employing both shadowgraphs and the technique of reference 8, on various models at the test Reynolds number. For all of the models, the boundary-layer flow was observed to be turbulent ahead of or in the region of the trip wires.

The axial forces were resolved to forebody and base coefficients. For the forebody coefficients, the measured axial forces were adjusted to account for the difference between the base pressures and an assumed condition of free-stream static pressure acting at the base of the model.

The results of reference 9 for models with cylindrical afterbodies and of reference 10 for models with flared afterbodies indicate that the presence of the sting may have a significant effect on base axial force. However, there is evidence in references 7 and 9 that the forebody axial force is not significantly affected. The magnitude of the sting interference on the base axial force is not known for the present models.

The angles of attack have been corrected for elastic deflection of the balance and sting under aerodynamic loads. Stream angularity corrections are negligible.

No corrections were made for possible interference effects of the perforated test-section walls, although the model base area was as much as 0.85 percent of the cross-sectional area of the test section. Such interference effects are believed to be relatively small, in view of the results of tests at transonic speeds of various sizes of sharp- and blunt-nosed bodies reported in the appendix to reference 11.

In addition to the possible systematic errors from neglecting some of the above corrections, certain random errors exist which influence the precision, or repeatability, of the results. The precision of the data was determined by the method described in reference 12 and the average deviations in values of Mach number, angle of attack, and aerodynamic coefficients presented herein were found to be approximately as follows:

M	$\pm 0.003$
$\alpha$	$\pm 0.05^\circ$
$C_N$	$\pm 0.02$
$C_m$	$\pm 0.03$
$C_{A_f}$	$\pm 0.02$
$C_{A_b}$	$\pm 0.01$

## RESULTS

The variations with angle of attack of coefficients of normal force, pitching moment, forebody axial force, and base axial force are presented in figures 3 to 5 for the various models of this investigation. Results are presented for both increasing and decreasing angles of attack for those models for which hysteresis loops appear in the variations of aerodynamic coefficients with angle of attack. This hysteresis phenomenon, which is associated with regions of separated flow, has been shown to be a common and undesirable feature of transonic flow over blunt-nosed bodies, since the introduction into the pitching cycle of the energy represented by the hysteresis loop may lead to large pitching oscillations (ref. 7).

In figures 6 and 7, respectively, are summarized the variations with Mach number of  $C_N/\alpha$  and c.p. location at three selected angles of attack. In figure 8 are presented the forebody and base axial-force coefficients at  $0^\circ$  angle of attack.

Shadowgraph pictures are presented in figures 9 and 10 to show the effect of the flow deflectors on the flow about the models with flared afterbodies.

It is interesting to note that for the model without flare, use of the flow deflectors resulted generally in (1) no significant effect on the normal-force parameter, (2) a major reduction in center-of-pressure travel with Mach number at small angles of attack, and (3) considerable reductions in the forebody axial-force coefficient. On the other hand, for the models with afterbody flare, use of the flow deflectors resulted generally in (1) sizable reductions in normal-force parameter at low angles of attack as well as a more linear variation of  $C_N$  with  $\alpha$ , (2) no significant change in the center-of-pressure travel with Mach number, (3) a forward shift in center of pressure at low angles of attack resulting in essentially a constant c.p. location with change in  $\alpha$ , and (4) various effects on the forebody axial-force coefficient, ranging

from slight reductions to significant increases, depending on the particular flow deflector, spike length, and Mach number considered. Furthermore, the aforementioned results for the models with afterbody flare were essentially independent of flow deflector shape.

Ames Research Center  
National Aeronautics and Space Administration  
Moffett Field, May 12, 1961

#### REFERENCES

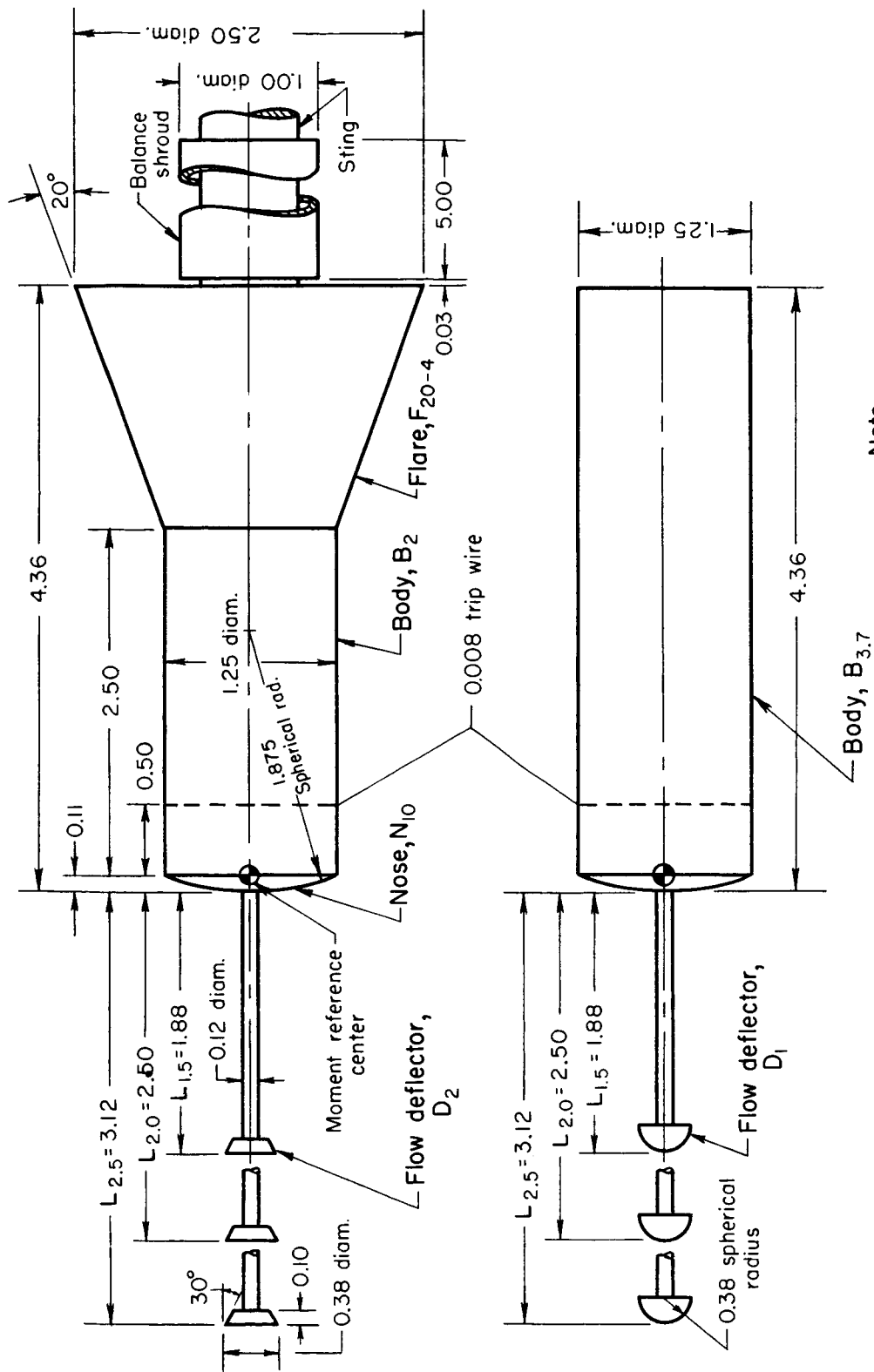
1. Knechtel, Earl D., Treon, Stuart L., and Wakefield, Roy M.: Transonic Static Aerodynamic Characteristics of a Blunt Cone-Cylinder Body With Flared Afterbody or Blunt Cruciform Fins. NASA TM X-40, 1959.
2. Wakefield, Roy M., Knechtel, Earl D., and Treon, Stuart L.: Transonic Static Aerodynamic Characteristics of a Blunt Cone-Cylinder Body With Flared Afterbodies of Various Angles and Base Areas. NASA TM X-106, 1959.
3. Knechtel, Earl D., Wakefield, Roy M., and Treon, Stuart, L.: Transonic Static Aerodynamic Characteristics of a Low-Fineness-Ratio Body of Revolution Having a Blunt Ellipsoidal Nose and Flared Afterbodies of Various Angles and Base Areas. NASA TM X-113, 1959.
4. Treon, Stuart L., Wakefield, Roy M., and Knechtel, Earl D.: Effects of Nose Shape and Afterbody Flare on the Transonic Characteristics of a Low-Fineness-Ratio Body of Revolution. NASA TM X-164, 1960.
5. Wakefield, Roy M., Treon, Stuart L., and Knechtel, Earl D.: Effects of Centerbody Length and Nose Shape on the Transonic Characteristics of Low-Fineness-Ratio Bodies of Revolution With a Flared Afterbody. NASA TM X-366, 1960.
6. Spiegel, Joseph M., and Lawrence, Leslie F.: A Description of the Ames 2- by 2-Foot Transonic Wind Tunnel and Preliminary Evaluation of Wall Interference. NACA RM A55I21, 1956.
7. Reese, David E., Jr., and Wehrend, William R., Jr.: An Investigation of the Static and Dynamic Aerodynamic Characteristics of a Series of Blunt-Nosed Cylinder-Flare Models at Mach Numbers From 0.65 to 2.20. NASA TM X-110, 1959.

8. Main-Smith, J. D.: Chemical Solids as Diffusible Coating Films for Visual Indication of Boundary-Layer Transition in Air and Water. R and M No. 2755, British, A.R.C., 1954.
9. Lee, George, and Summers, James L.: Effects of Sting-Support Interference on the Drag of an Ogive-Cylinder Body With and Without a Boattail at 0.6 to 1.4 Mach Number. NACA RM A57109, 1957.
10. Reese, David E., Jr., and Wehrend, William R., Jr.: Effects of Sting-Support Interference on the Base Pressures of a Model Having a Blunt-Nosed Cylinder Body and a Conical Flare at Mach Numbers of 0.65 to 2.20. NASA TM X-161, 1960.
11. Treon, Stuart L.: The Effect of Nose Shape on the Static Aerodynamic Characteristics of Ballistic-Type Missile Models at Mach Numbers From 0.6 to 1.4. NASA MEMO 5-17-59A, 1959.
12. Beers, Yardley: Introduction to the Theory of Error. Addison-Wesley Pub. Co., Cambridge, Mass., 1953.

[REDACTED]

A  
4  
1  
0

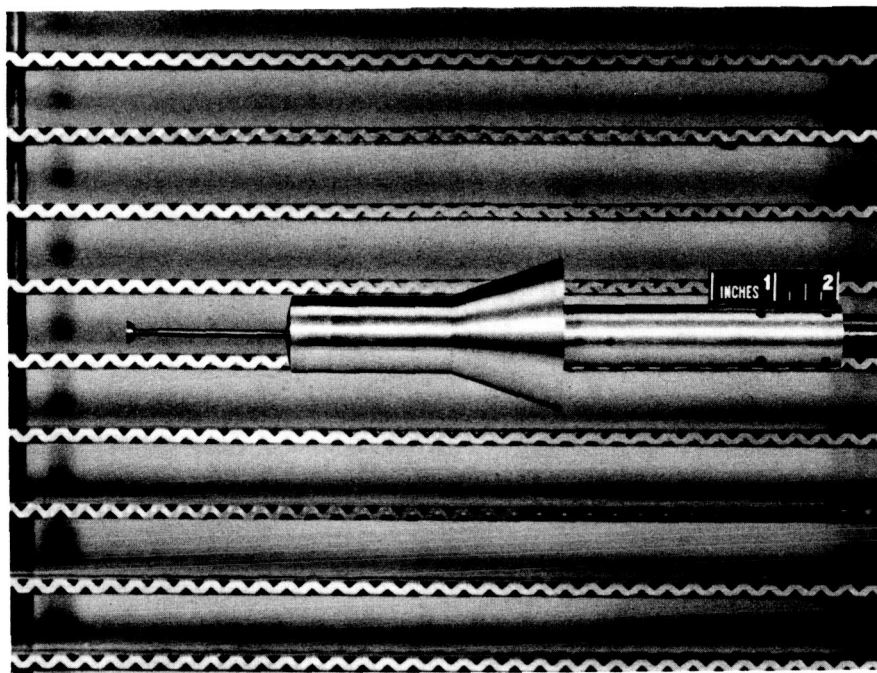
[REDACTED]



Note:

Dimensions in inches

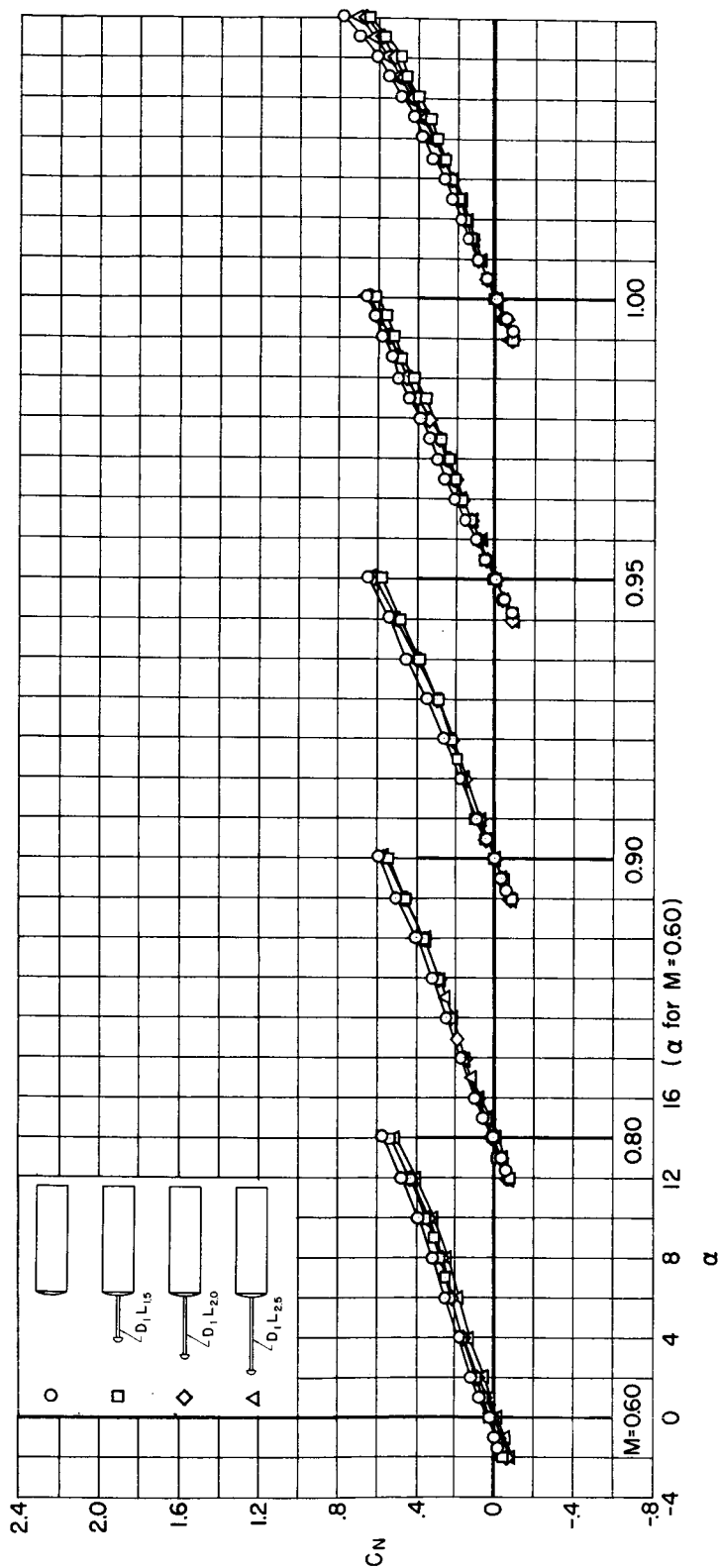
Figure 1.- Model sketches and dimensions.

~~CONFIDENTIAL~~

A-24668

Figure 2.- Model with a flow deflector installed in the test section of the 2- by 2-foot transonic wind tunnel.

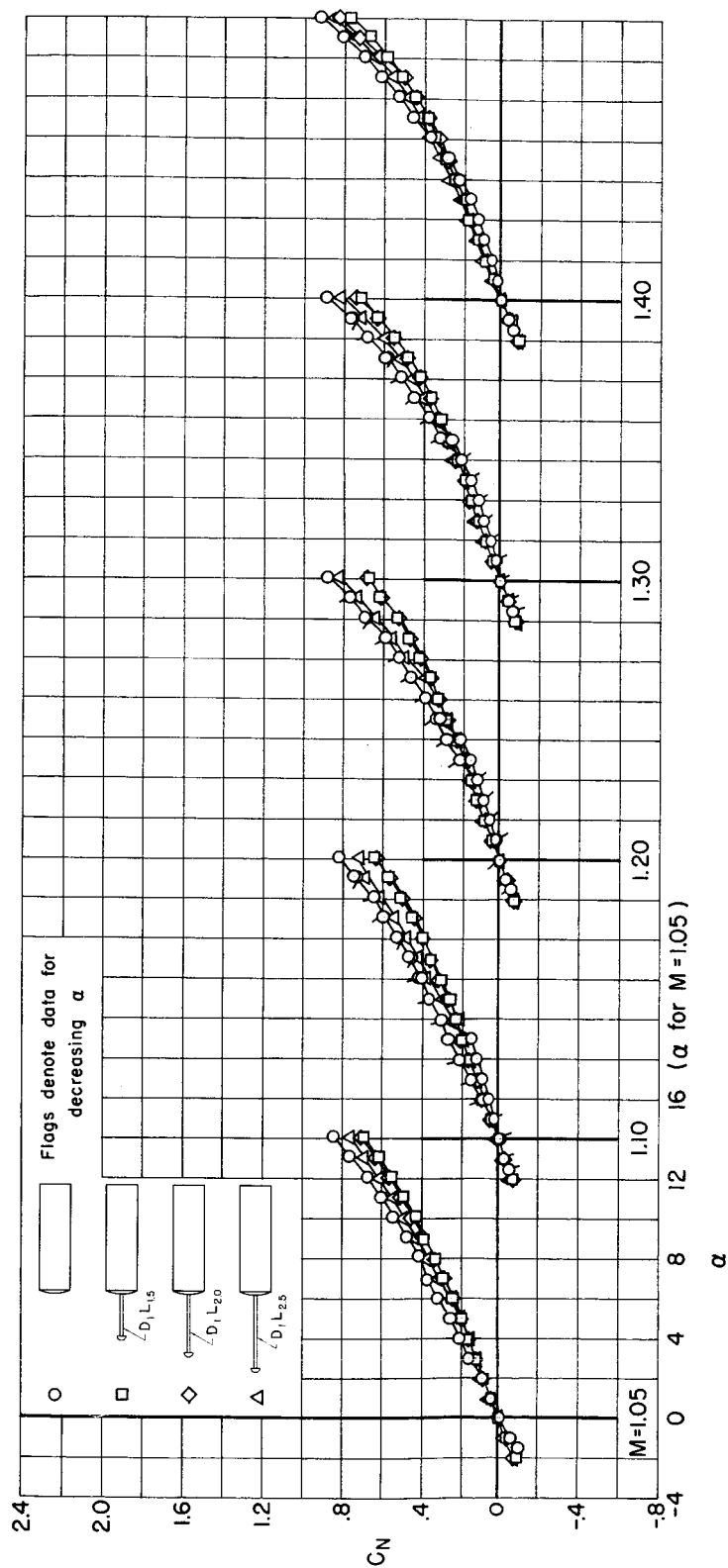
A  
4  
1  
0



(a) Normal-force coefficient;  $M = 0.60$  to  $1.00$ .

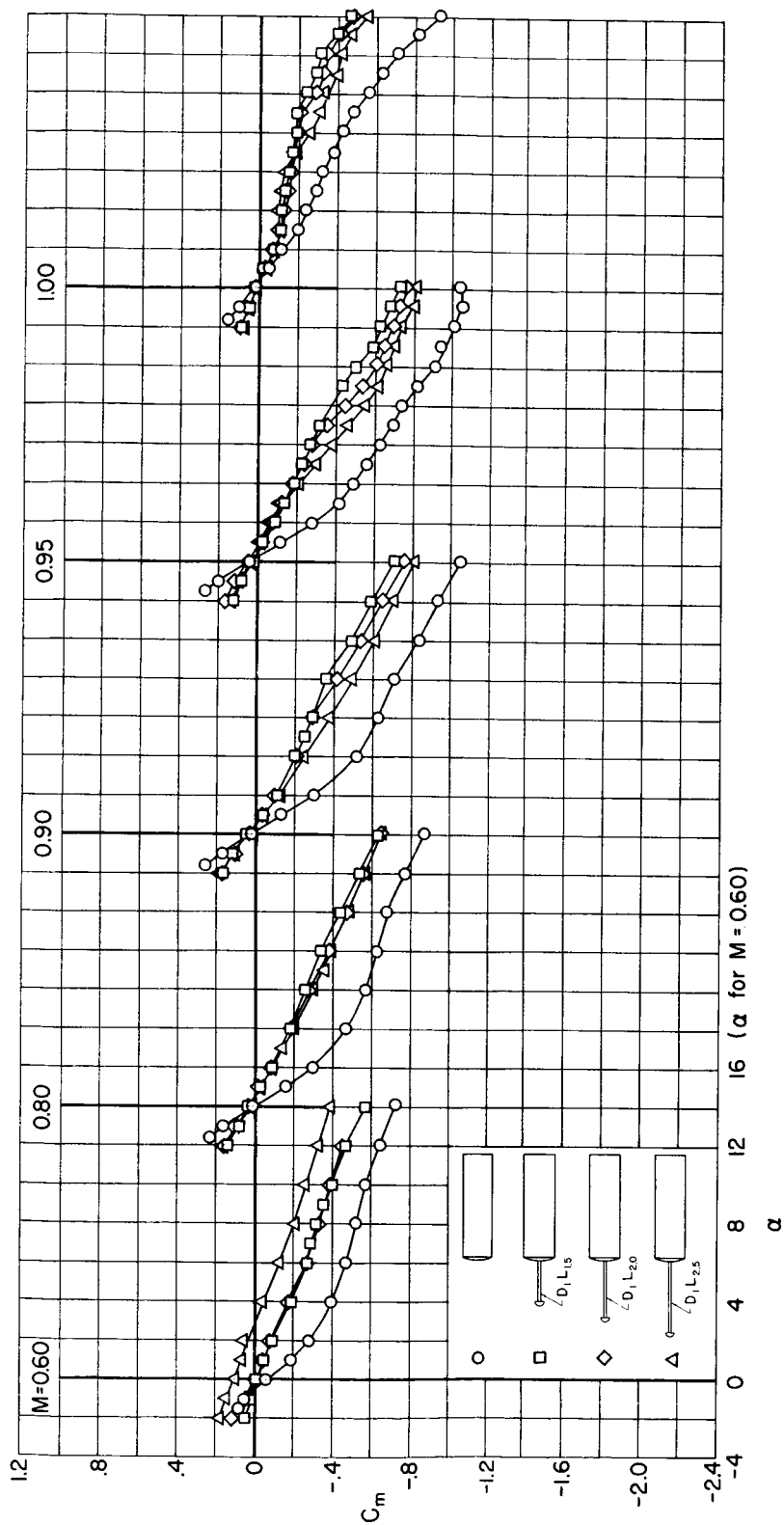
Figure 3.- Static longitudinal aerodynamic coefficients for the unflared models with hemispherical-shaped flow deflectors.





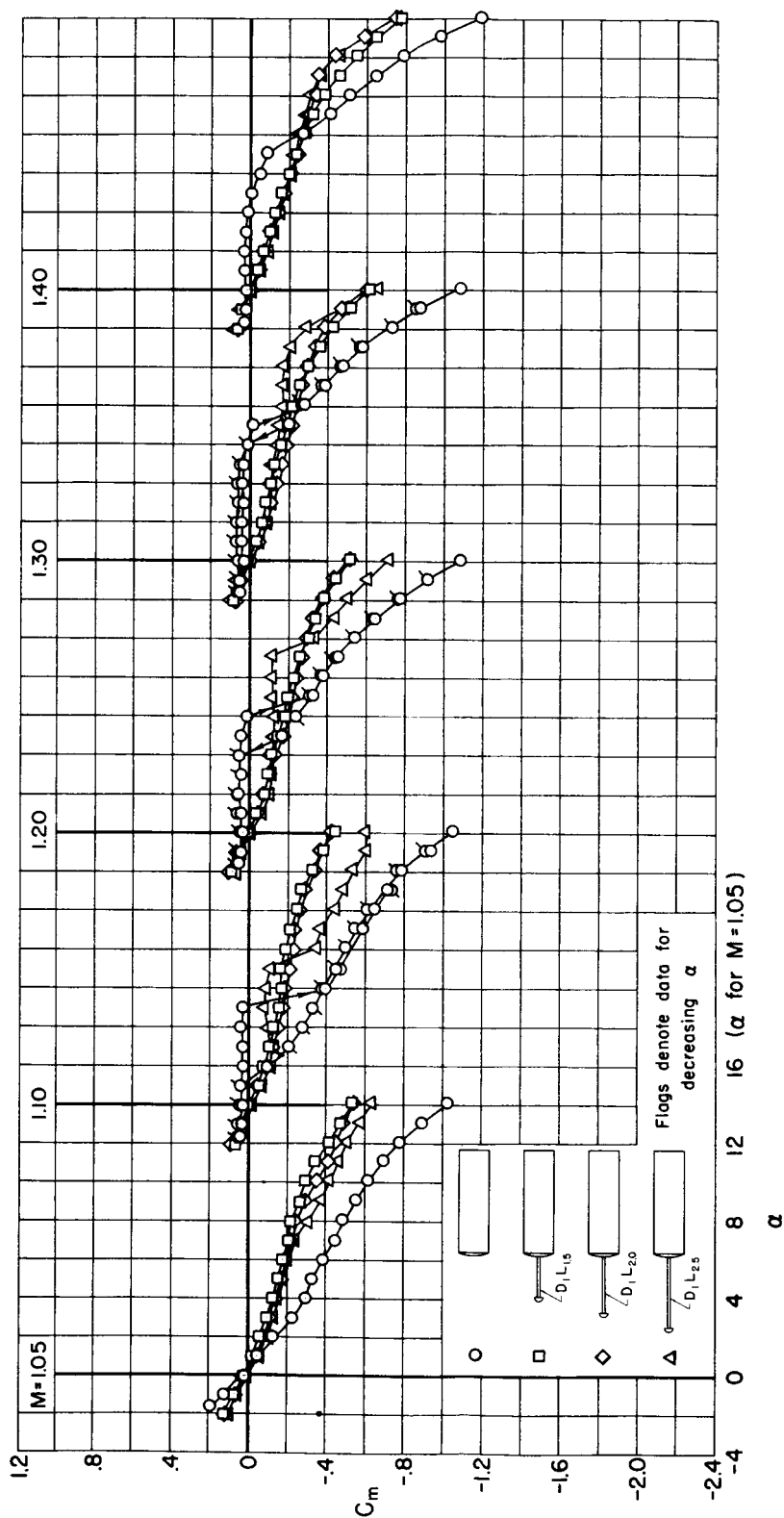
(b) Normal-force coefficient;  $M = 1.05$  to  $1.40$ .

Figure 3.- Continued.



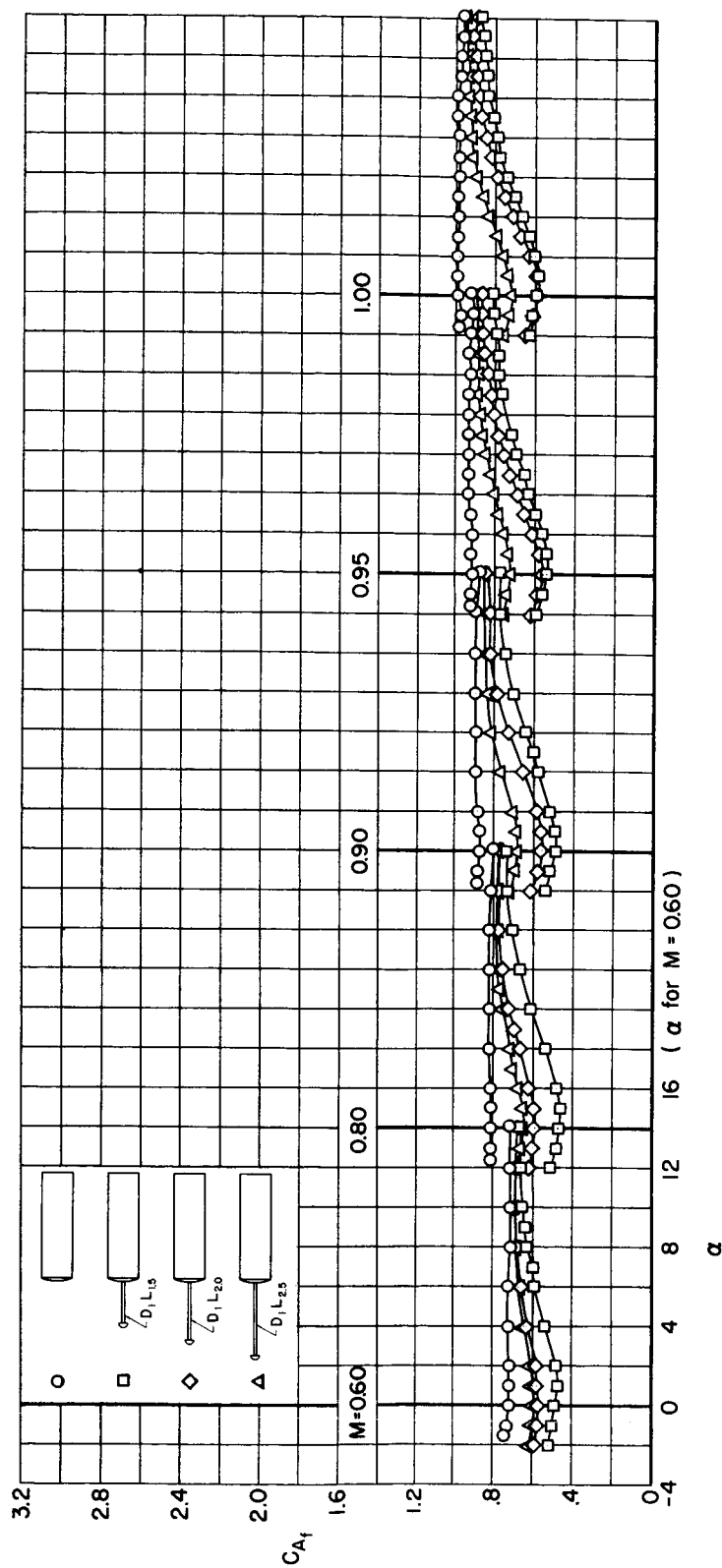
(c) Pitching-moment coefficient;  $M = 0.60$  to  $1.00$ .

Figure 3.- Continued.



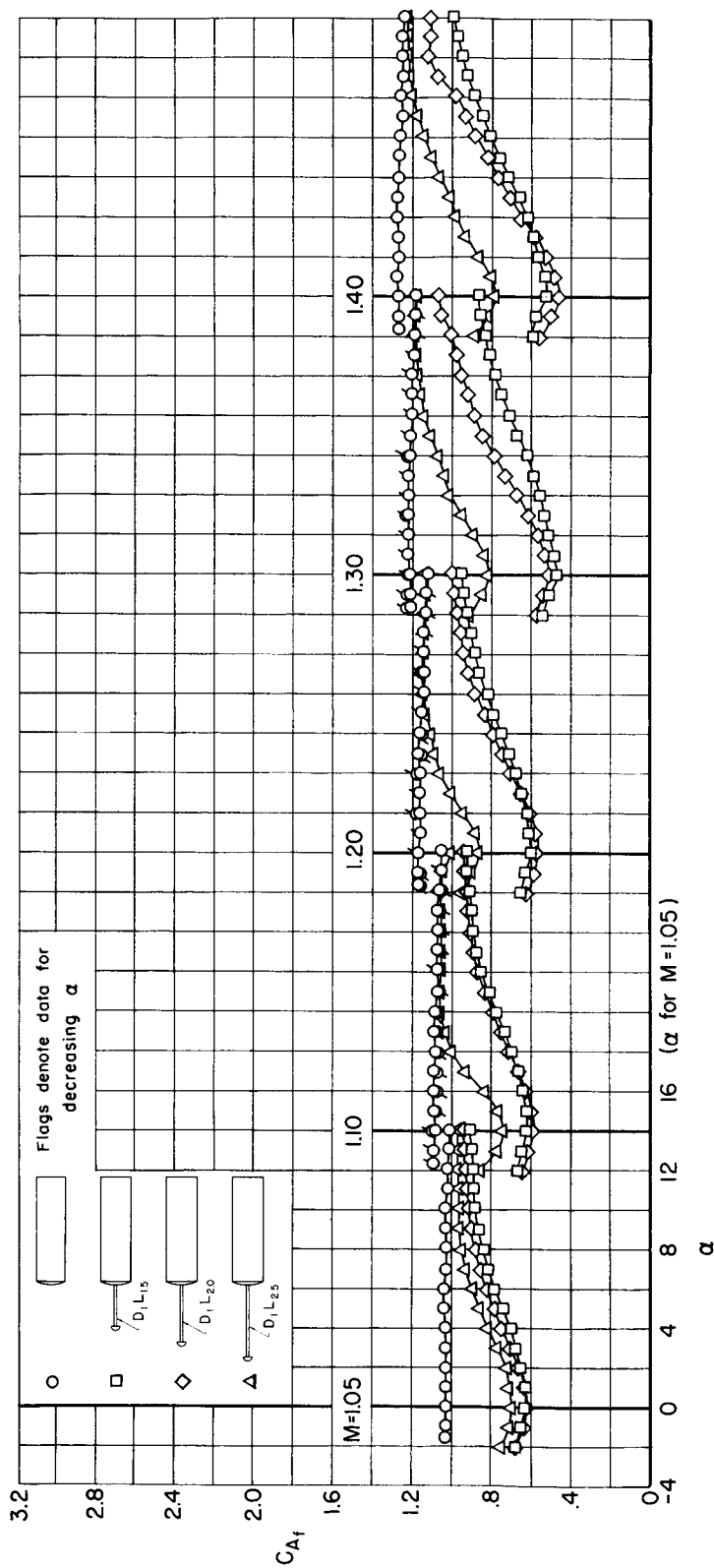
(d) Pitching-moment coefficient;  $M = 1.05$  to  $1.40$ .

Figure 3.- Continued.



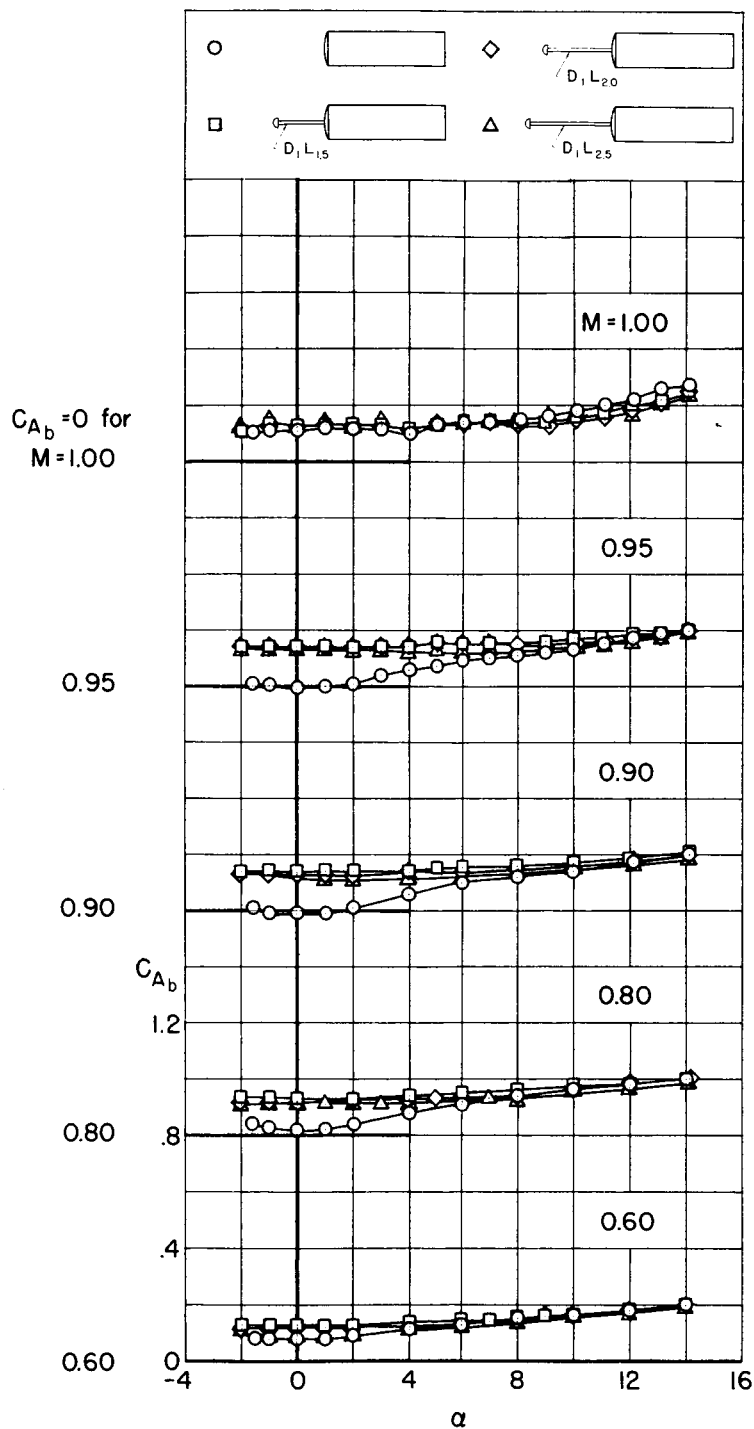
(e) Forebody axial-force coefficient;  $M = 0.60$  to  $1.00$ .

Figure 3.- Continued.



(f) Forebody axial-force coefficient;  $M = 1.05$  to  $1.40$ .

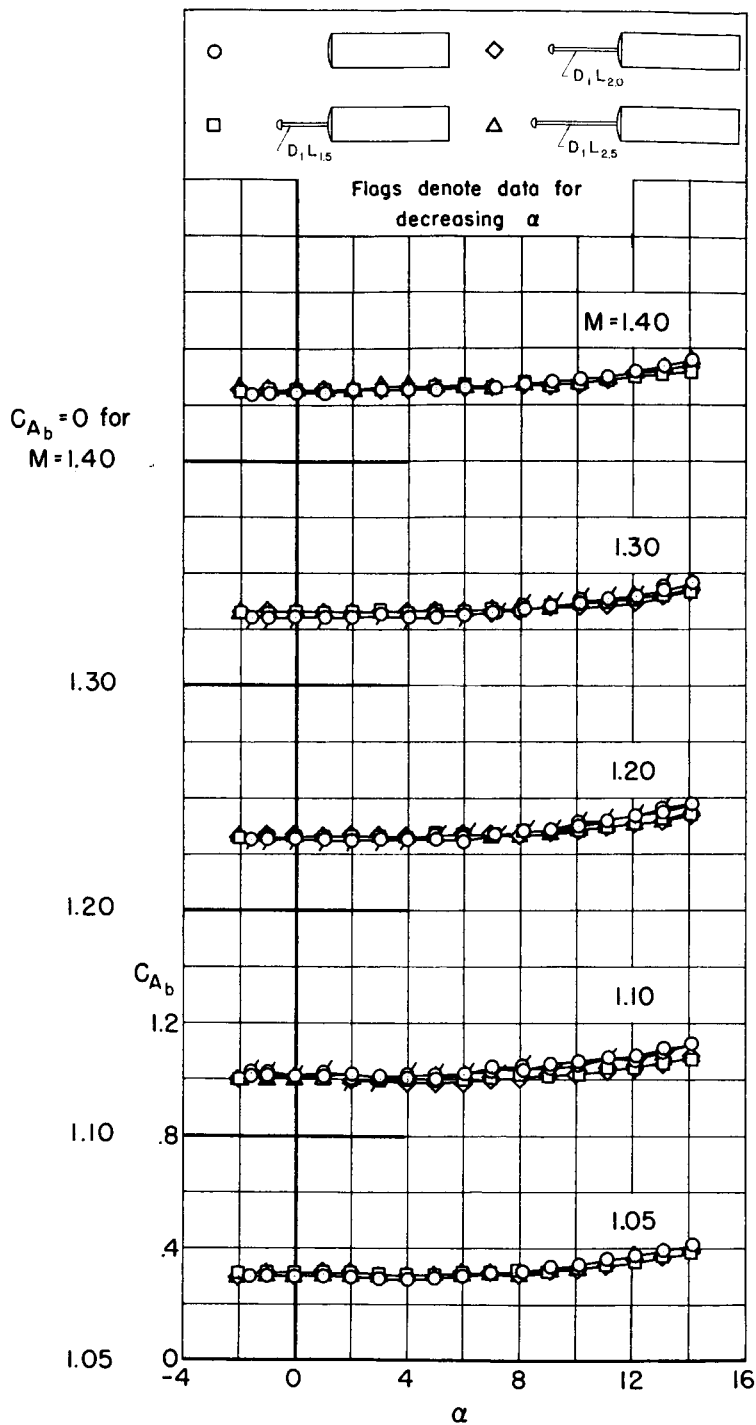
Figure 3.- Continued.



(g) Base axial-force coefficient;  $M = 0.60$  to  $1.00$ .

Figure 3.- Continued.

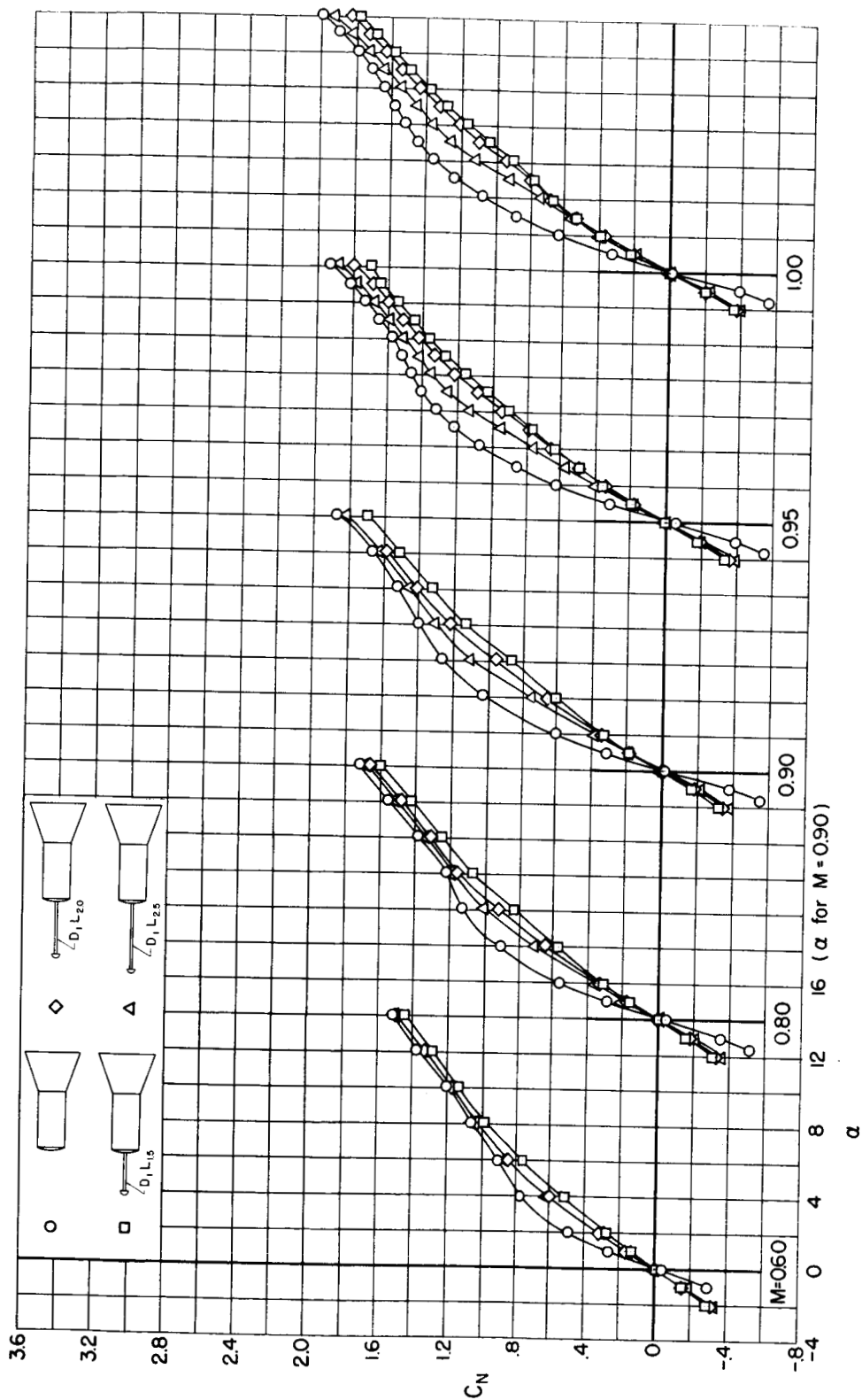
CONFIDENTIAL



(h) Base axial-force coefficient;  $M = 1.05$  to  $1.40$ .

Figure 3.- Concluded.

CONFIDENTIAL



(a) Normal-force coefficient;  $M = 0.60$  to  $1.00$ .

Figure 4.- Static longitudinal aerodynamic coefficients for the flared models with hemispherical-shaped flow deflectors.



CONFIDENTIAL

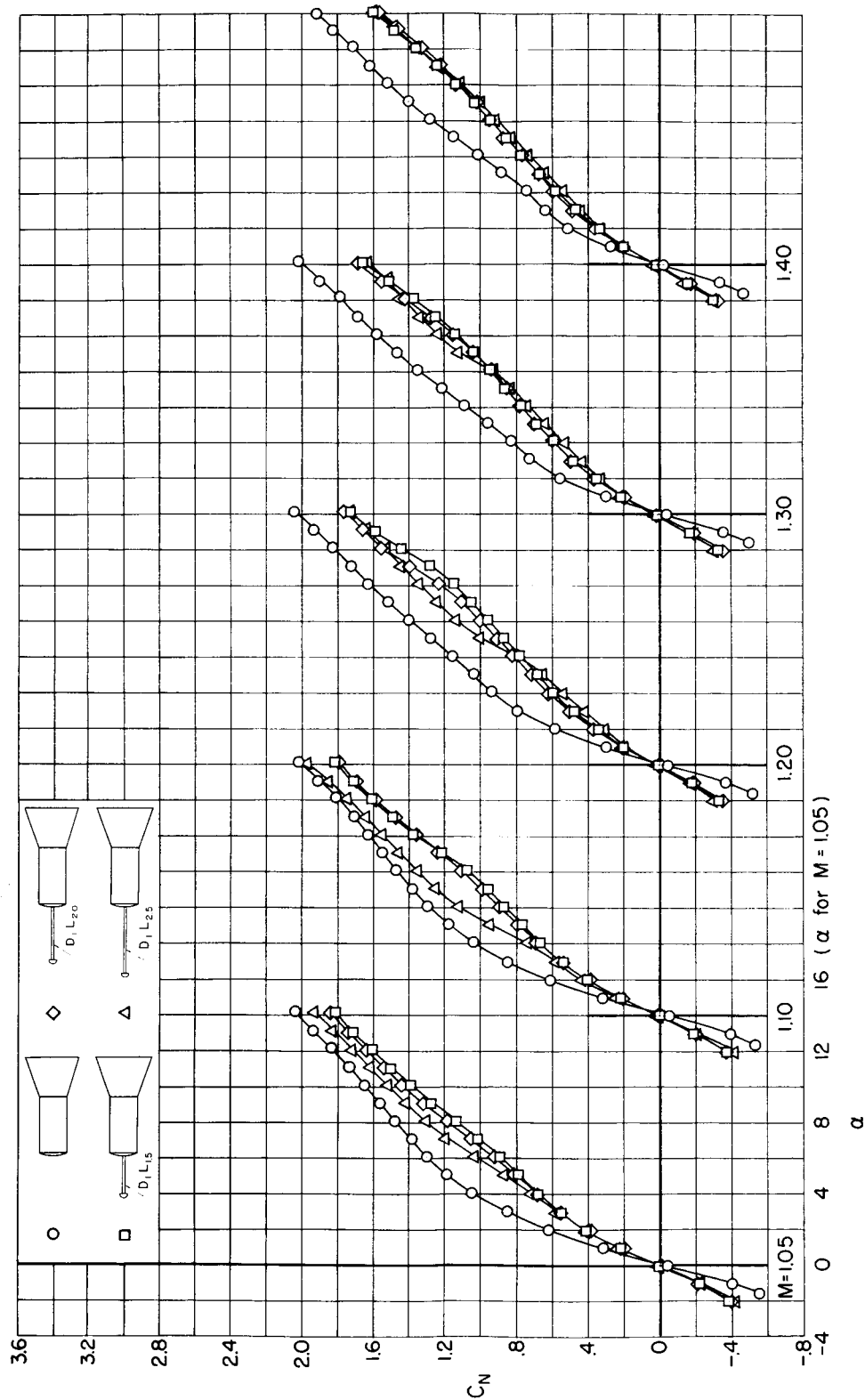
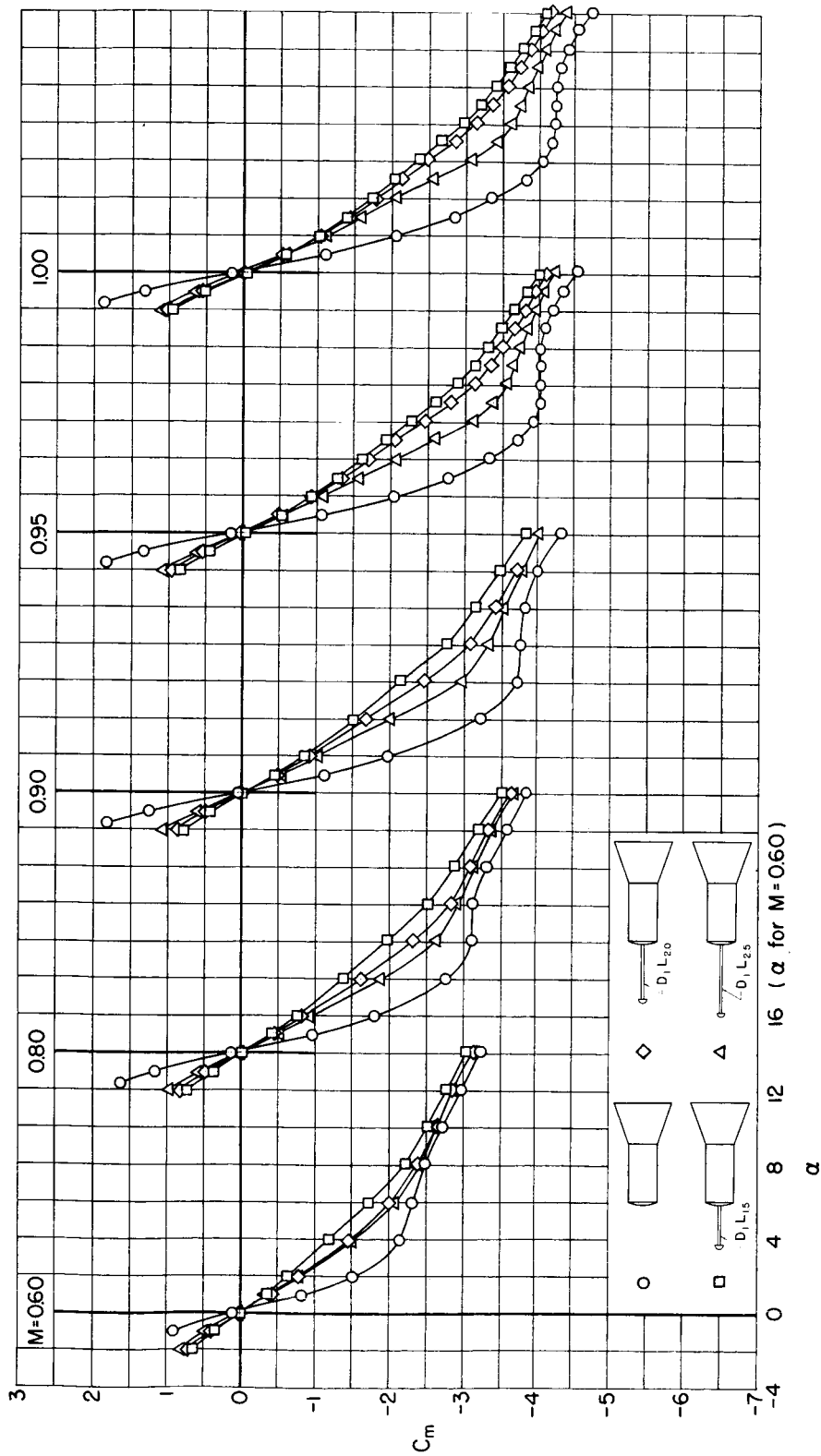
(b) Normal-force coefficient;  $M = 1.05$  to  $1.40$ .

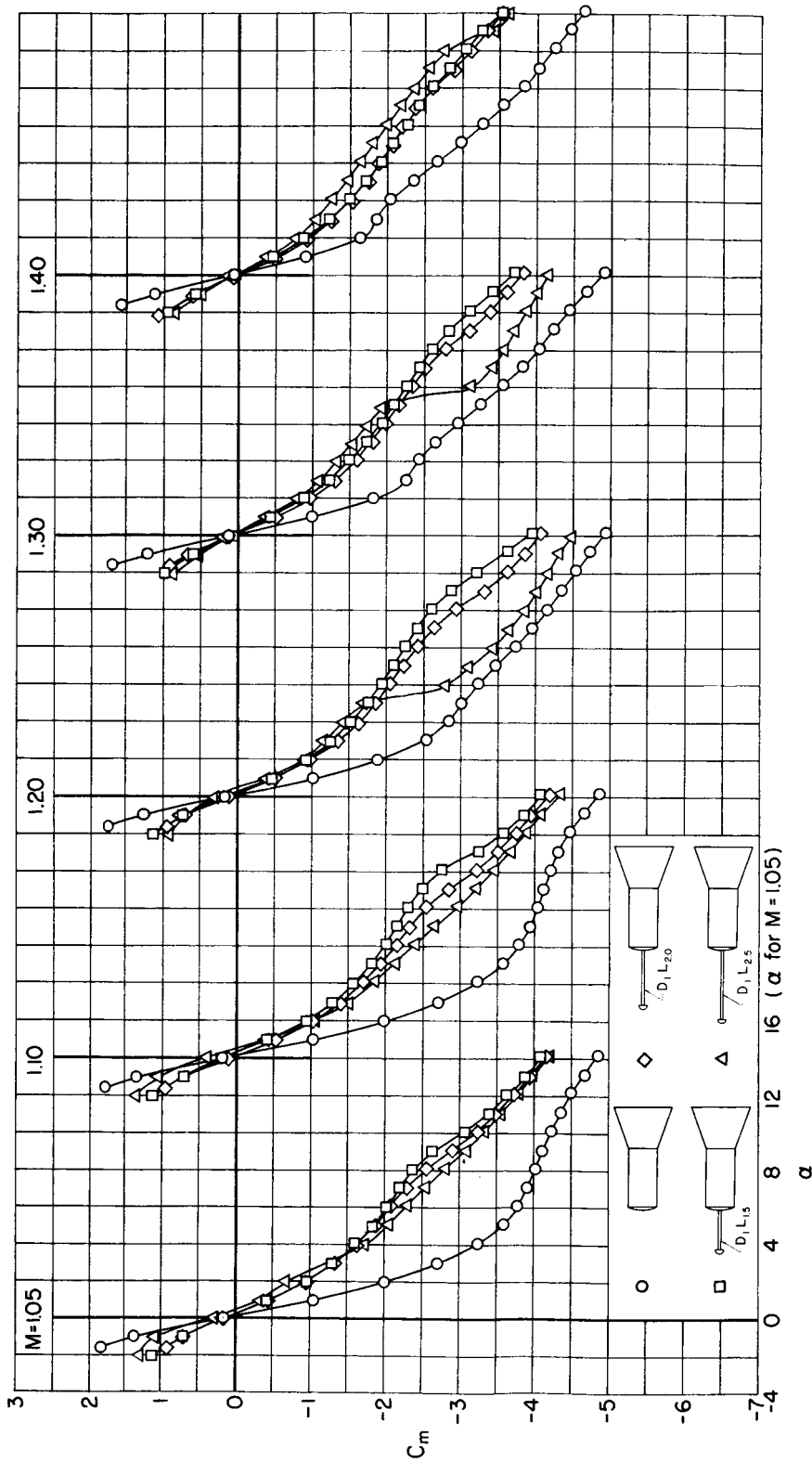
Figure 4.- Continued.

CONFIDENTIAL



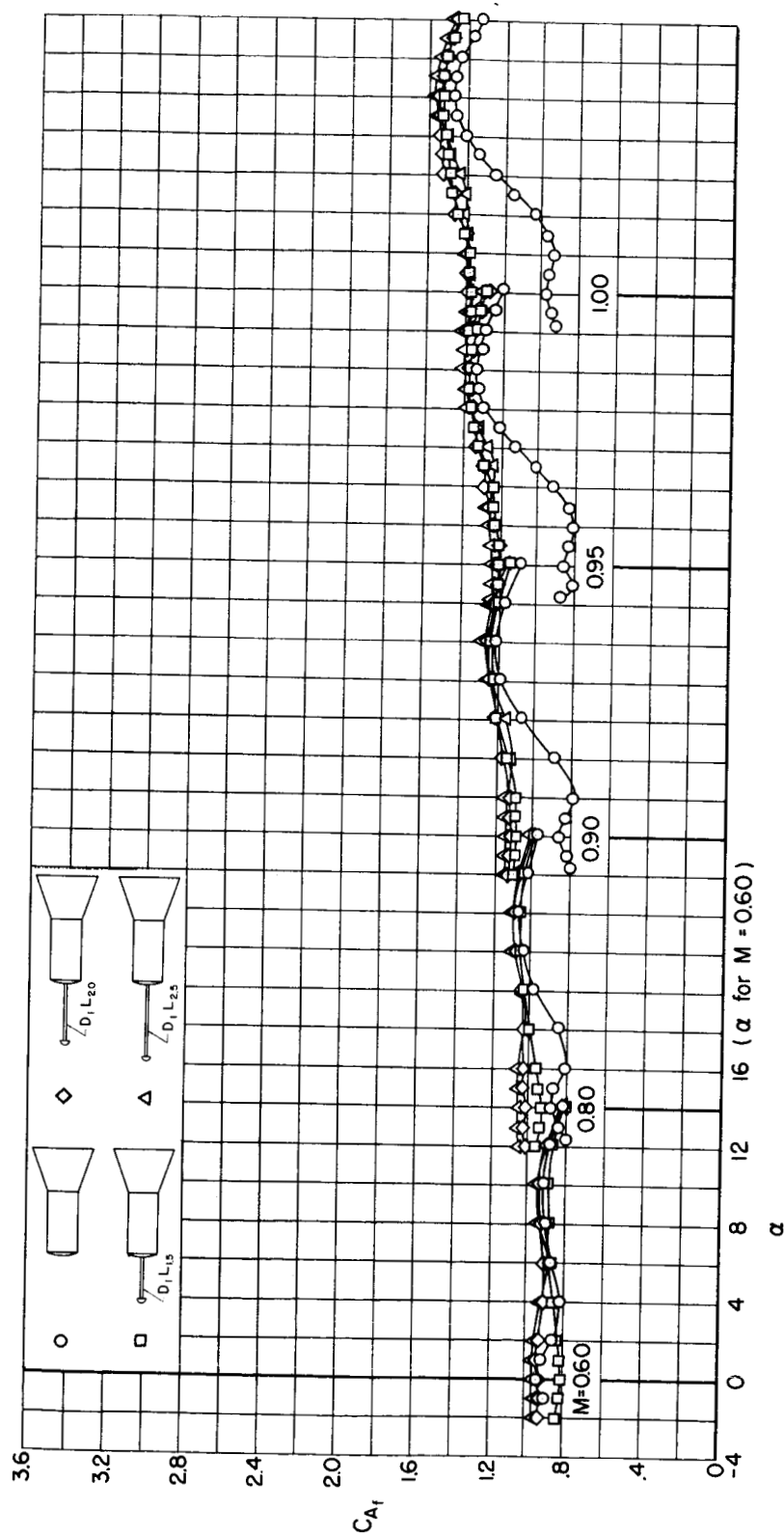
(c) Pitching-moment coefficient;  $M = 0.60$  to 1.00.

Figure 4.- Continued.



(d) Pitching-moment coefficient;  $M = 1.05$  to  $1.40$ .

Figure 4.- Continued.



(e) Forebody axial-force coefficient;  $M = 0.60$  to  $1.00$ .

Figure 4.- Continued.

CONFIDENTIAL

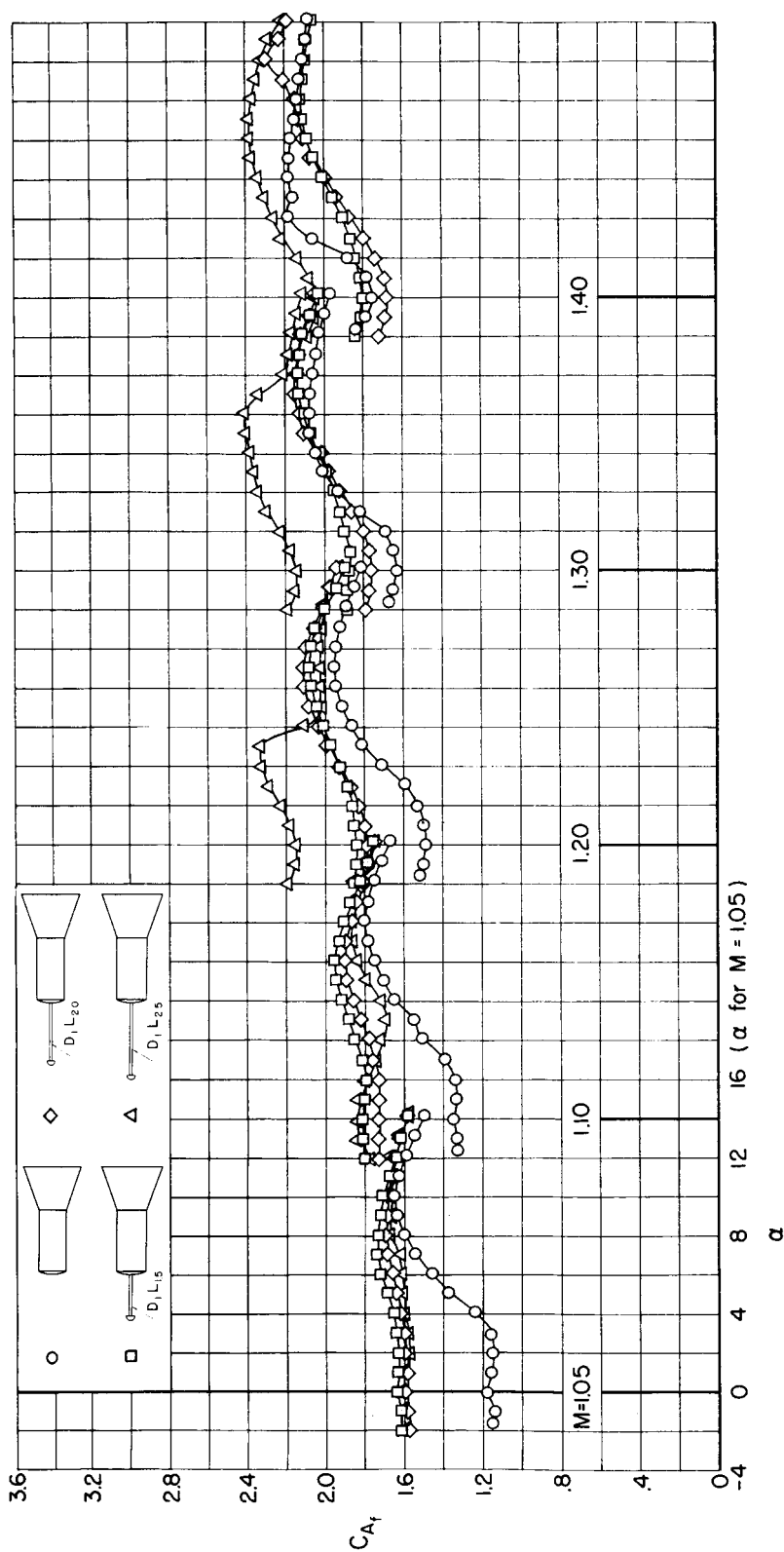
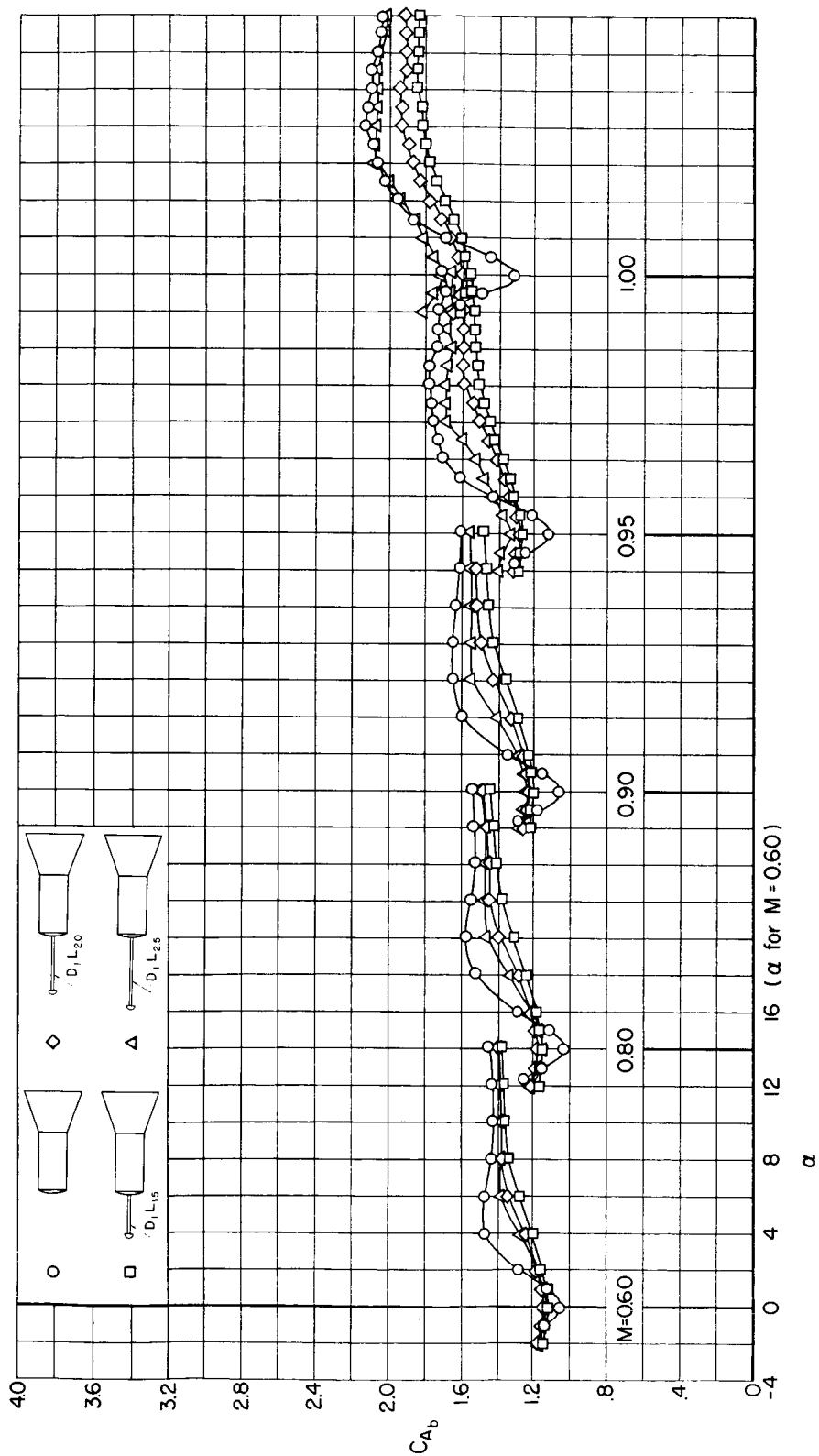
(f) Forebody axial-force coefficient;  $M = 1.05$  to  $1.40$ .

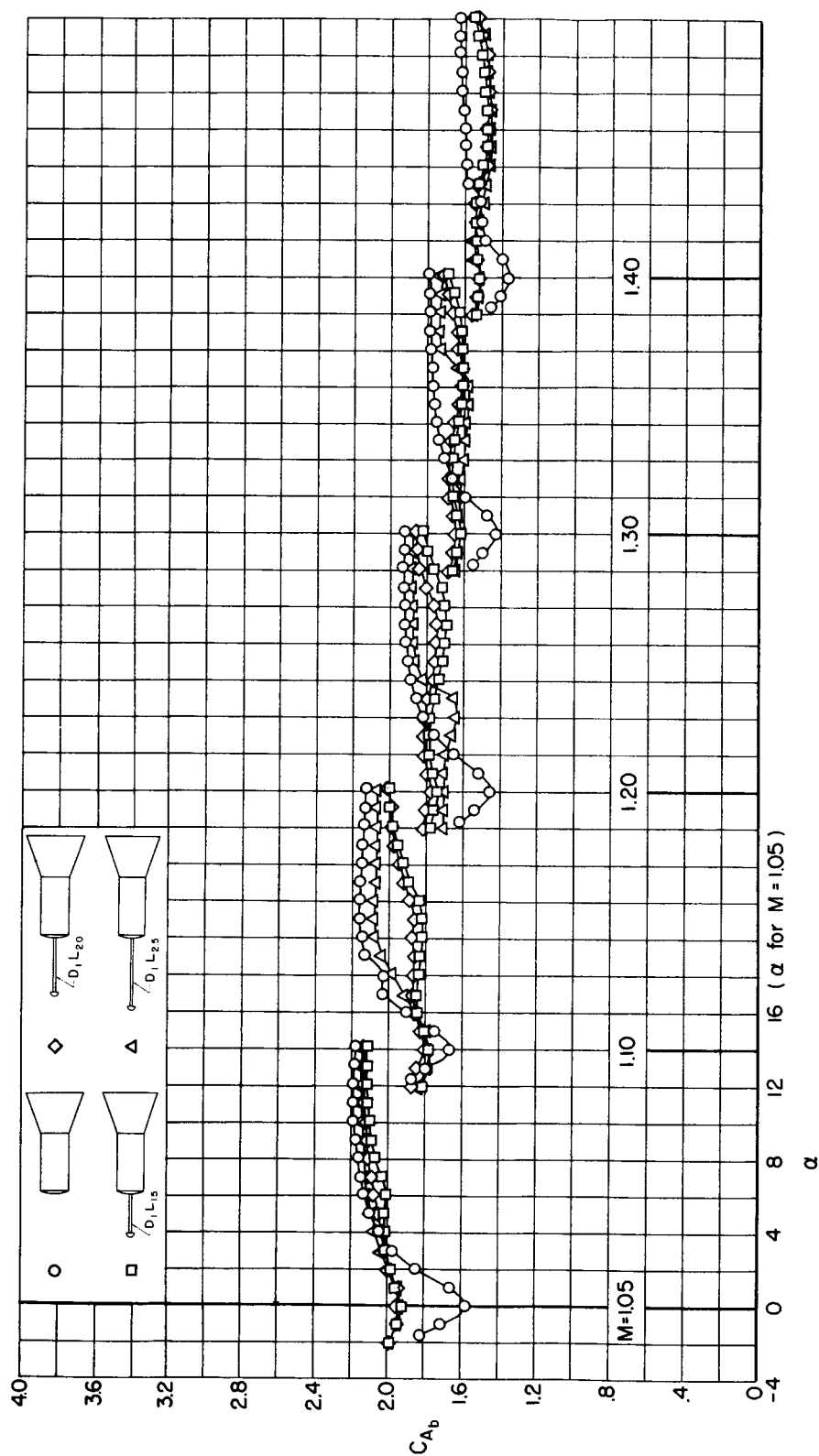
Figure 4.- Continued.

CONFIDENTIAL



(g) Base axial-force coefficient;  $M = 0.60$  to  $1.00$ .

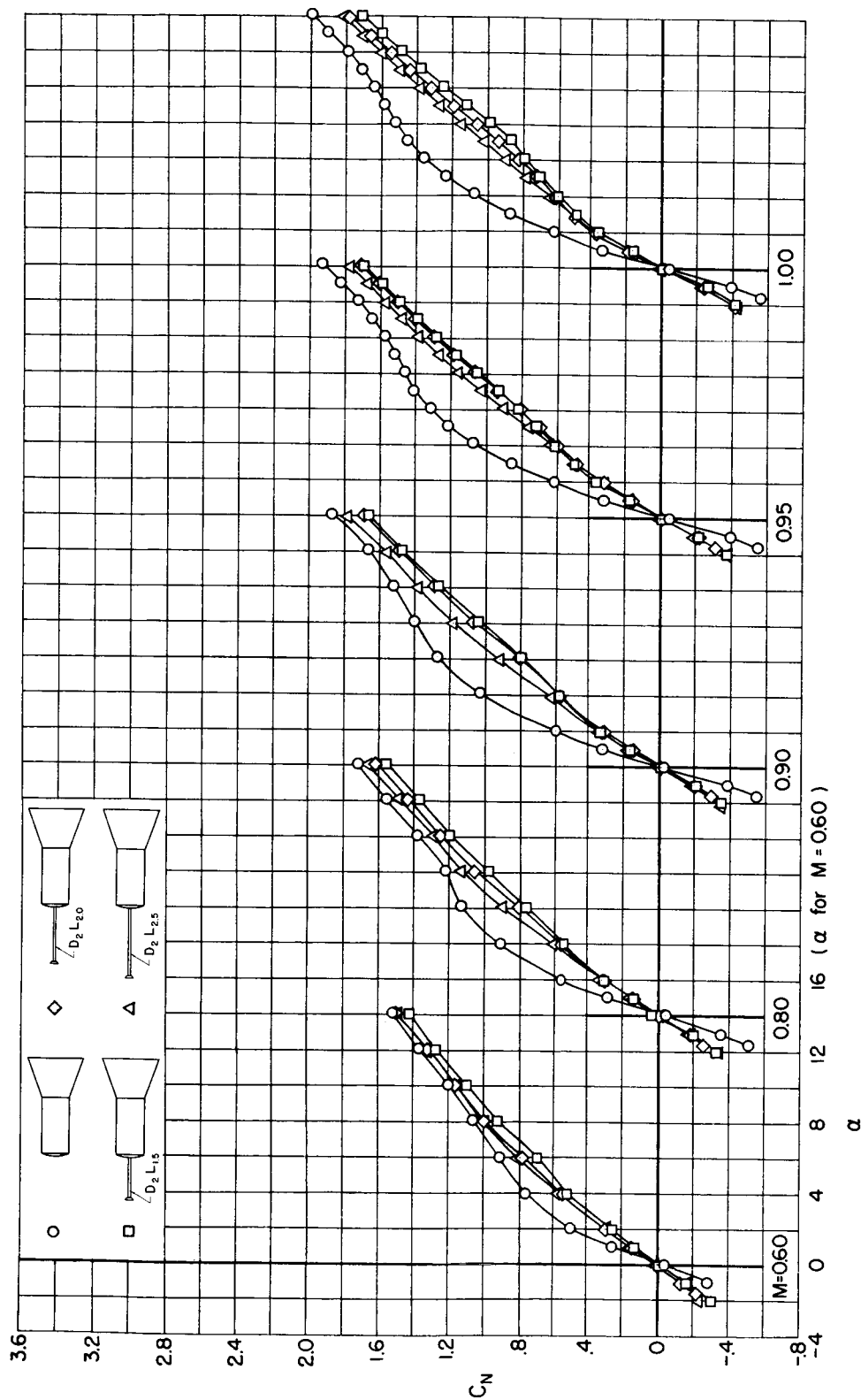
Figure 4.- Continued.



(h) Base axial-force coefficient;  $M = 1.05$  to  $1.40$ .

Figure 4.- Concluded.

CONFIDENTIAL



(a) Normal-force coefficient;  $M = 0.60$  to  $1.00$ .

Figure 5.- Static longitudinal aerodynamic coefficients for the flared models with disk-shaped flow deflectors.

CONFIDENTIAL



CONFIDENTIAL

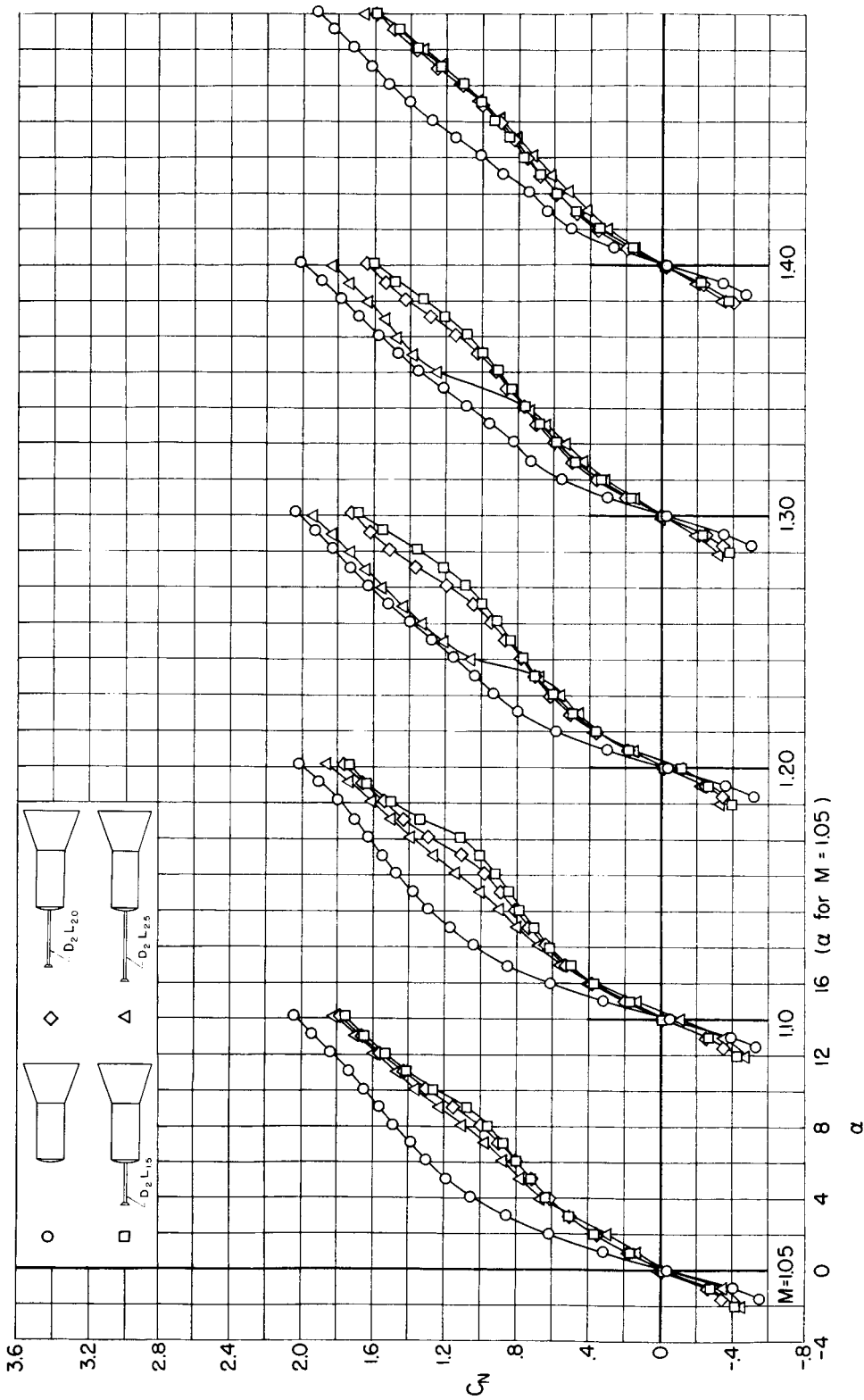
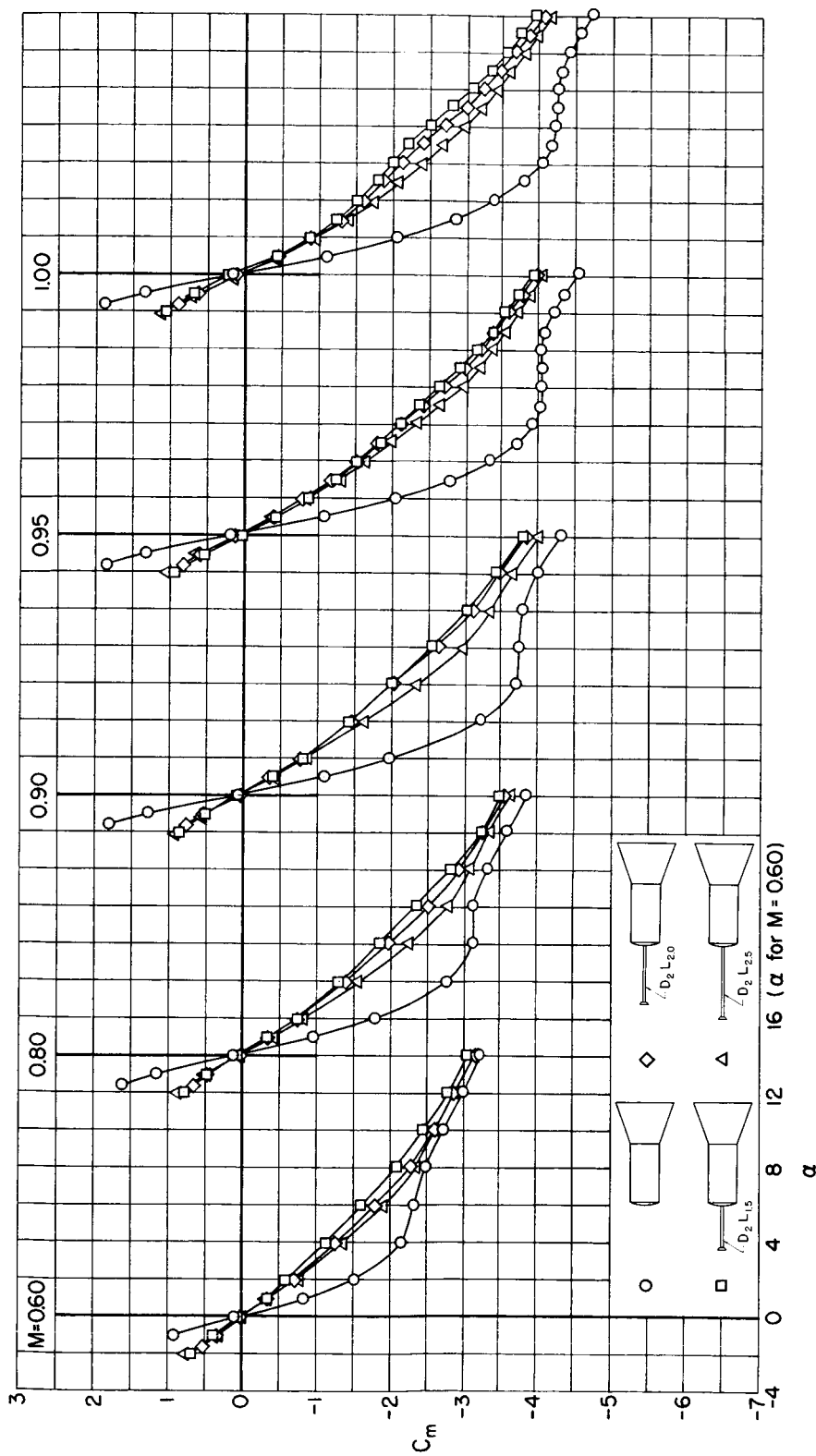
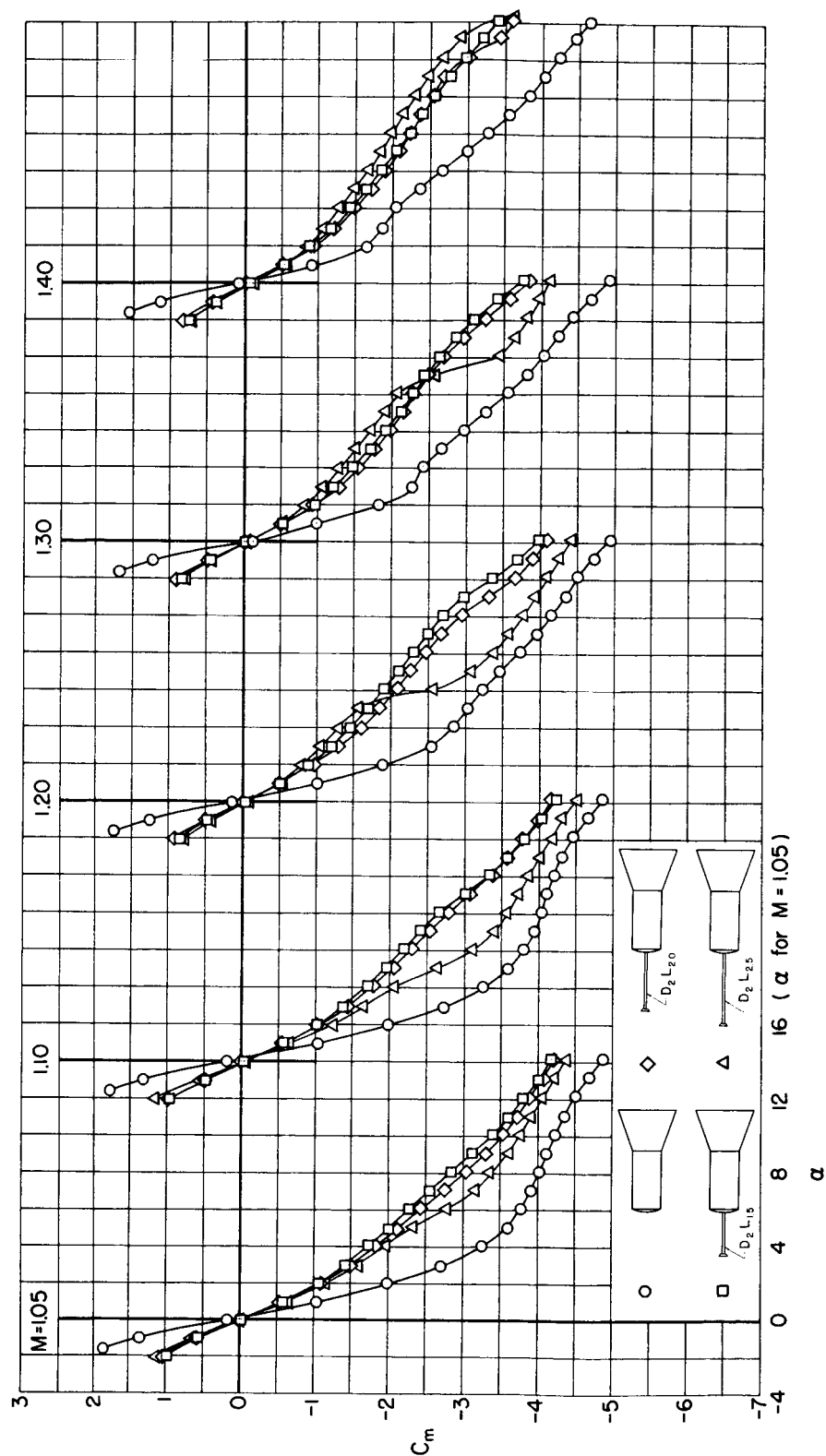
(b) Normal-force coefficient;  $M = 1.05$  to  $1.40$ .

Figure 5.- Continued.



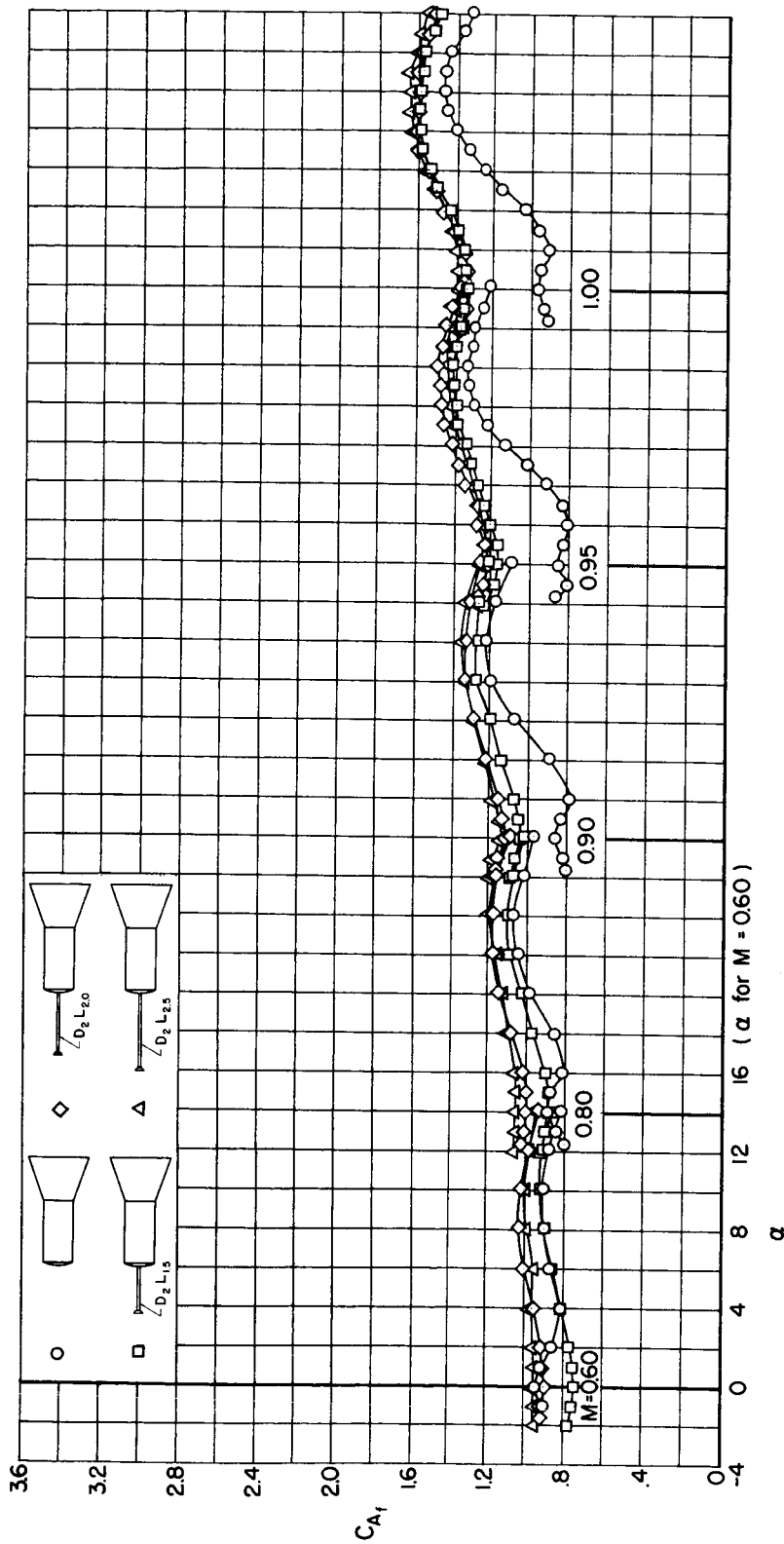
(c) Pitching-moment coefficient;  $M = 0.60$  to  $1.00$ .

Figure 5.- Continued.



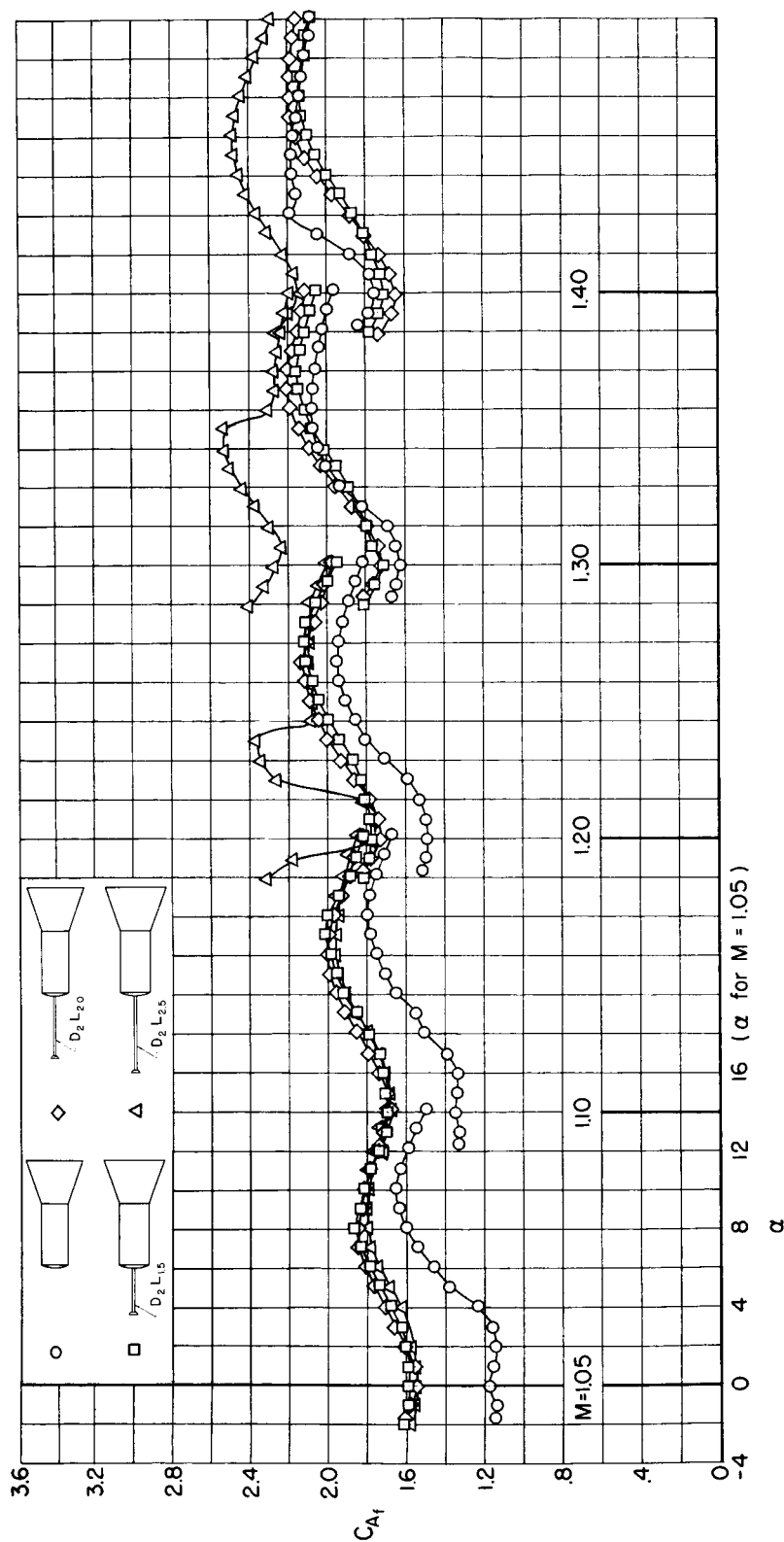
(d) Pitching-moment coefficient;  $M = 1.05$  to  $1.40$ .

Figure 5.- Continued.



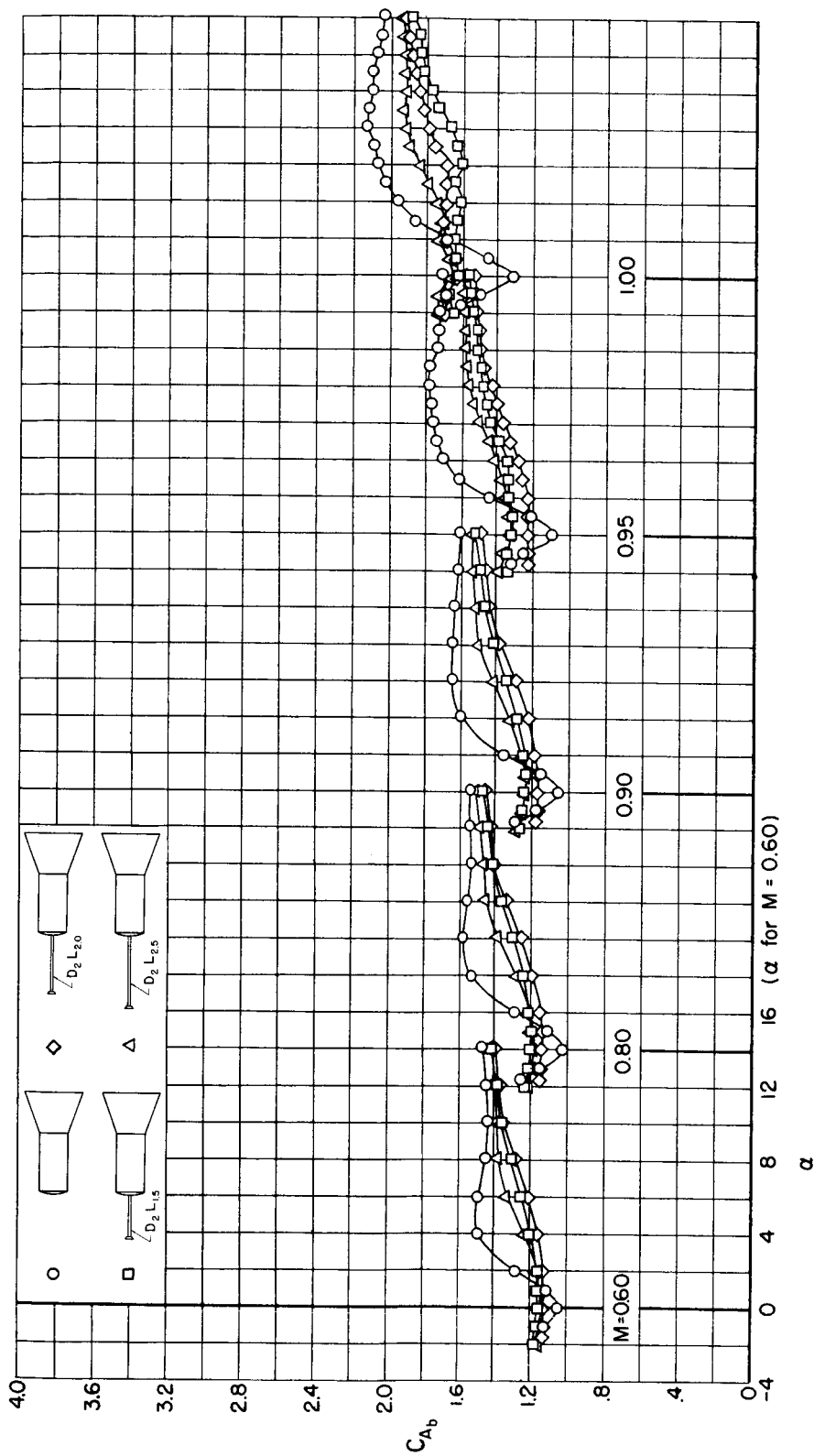
(e) Forebody axial-force coefficient;  $M = 0.60$  to  $1.00$ .

Figure 5.- Continued.



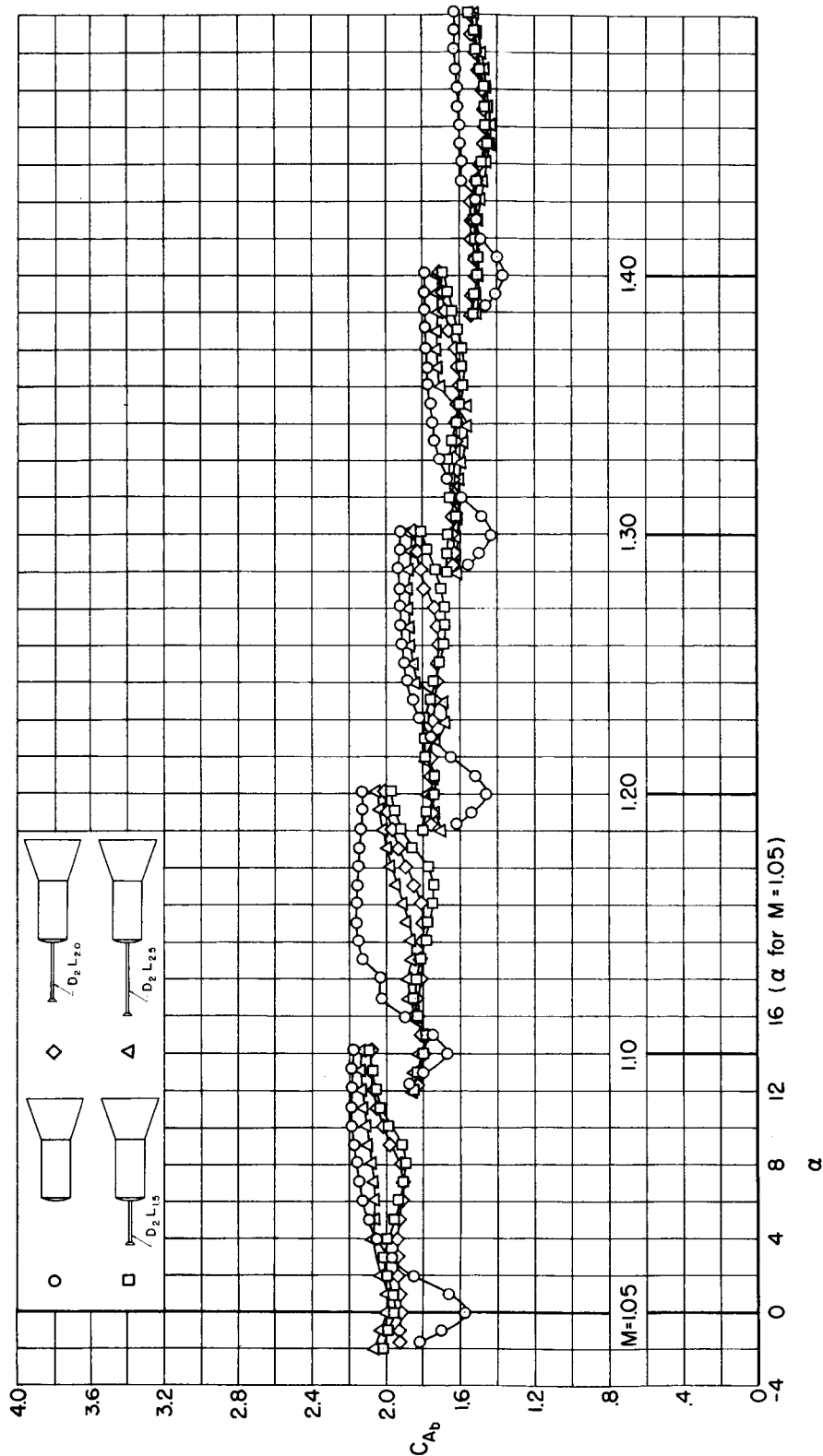
(f) Forebody axial-force coefficient;  $M = 1.05$  to 1.40.

Figure 5.- Continued.



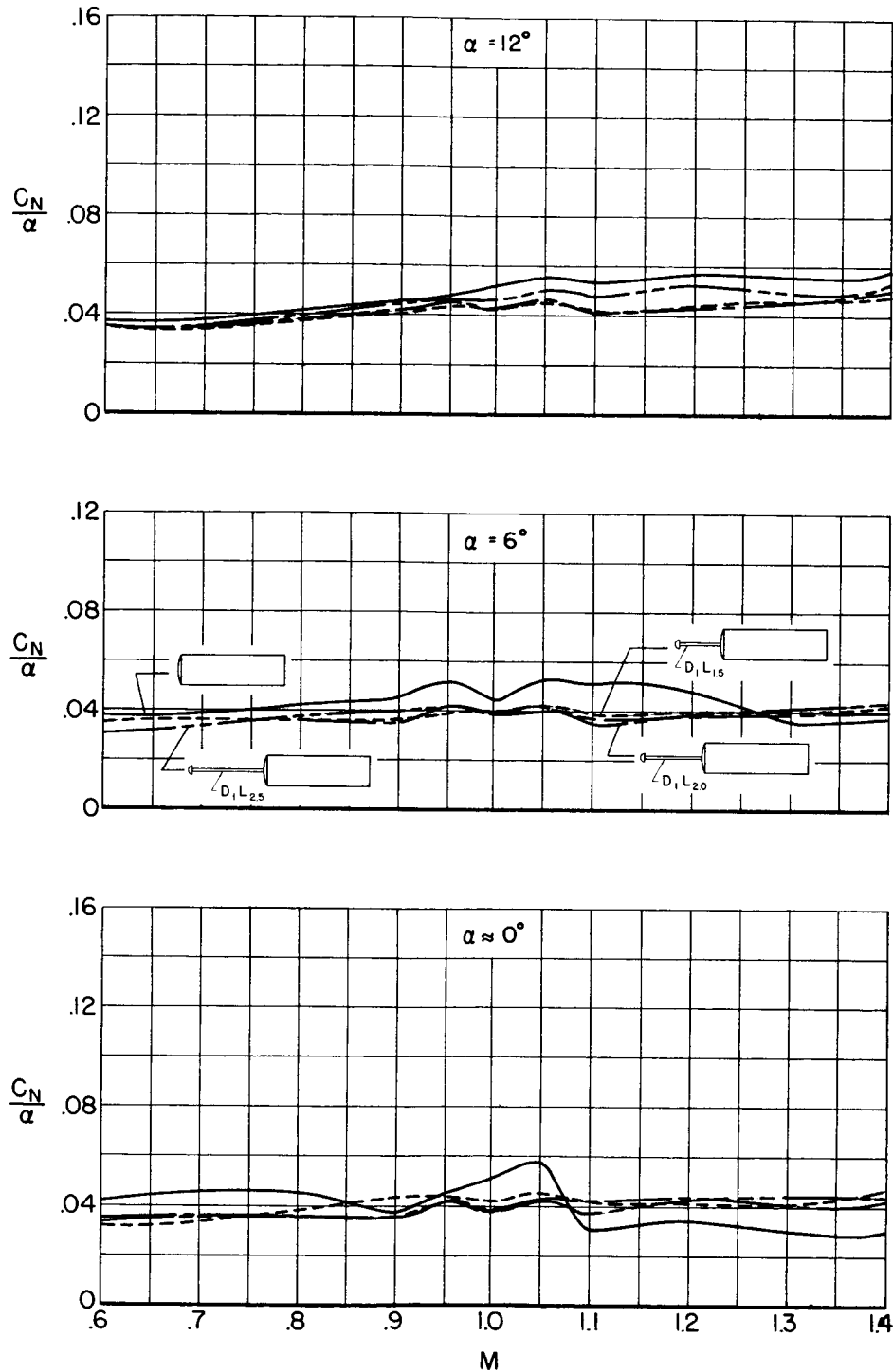
(g) Base axial-force coefficient;  $M = 0.60$  to  $1.00$ .

Figure 5.- Continued.



(h) Base axial-force coefficient;  $M = 1.05$  to  $1.40$ .

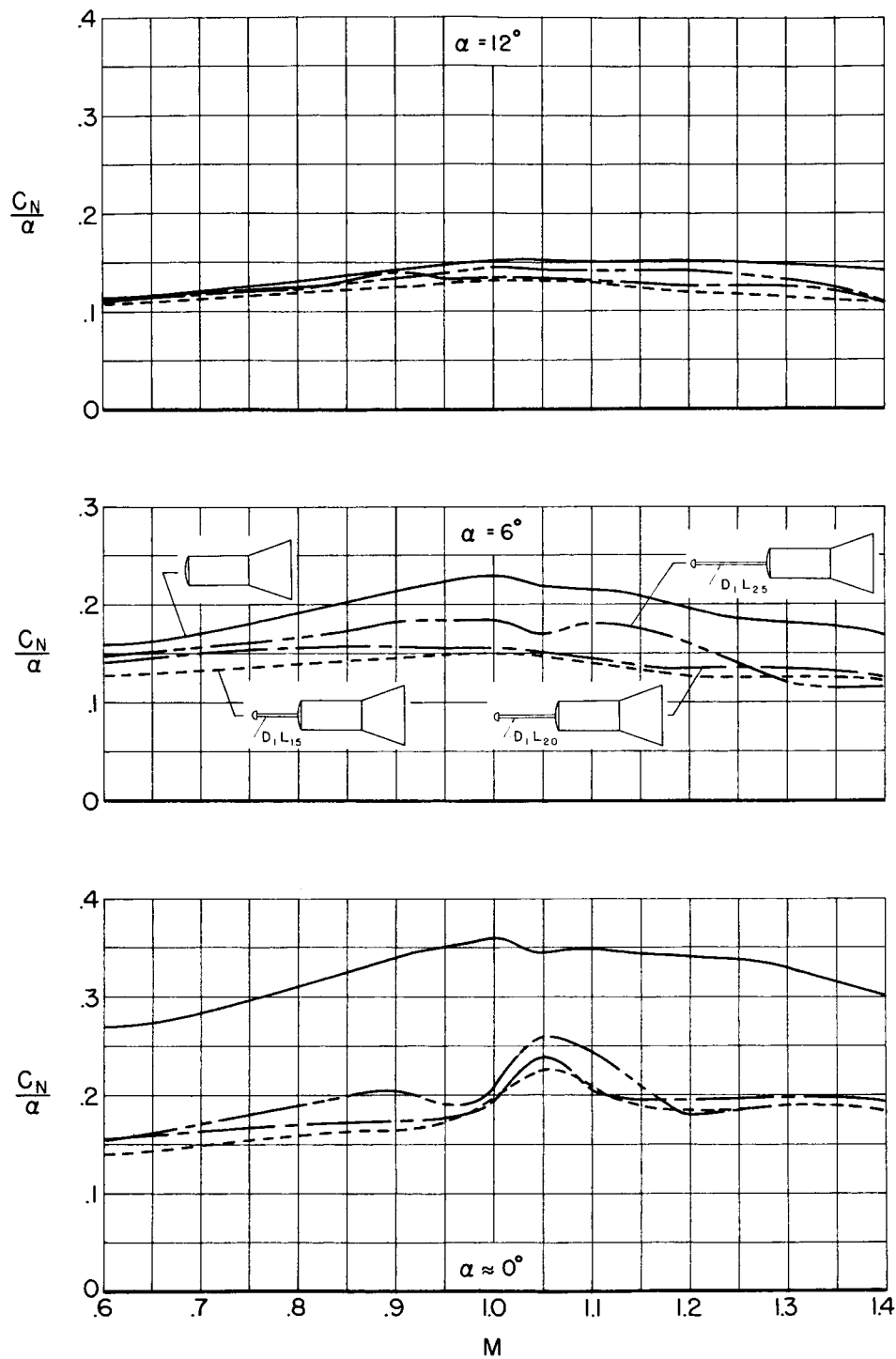
Figure 5.- Concluded.



(a) Unflared models with hemispherical deflector.

Figure 6.- Effects of flow deflector length on the normal-force parameter.

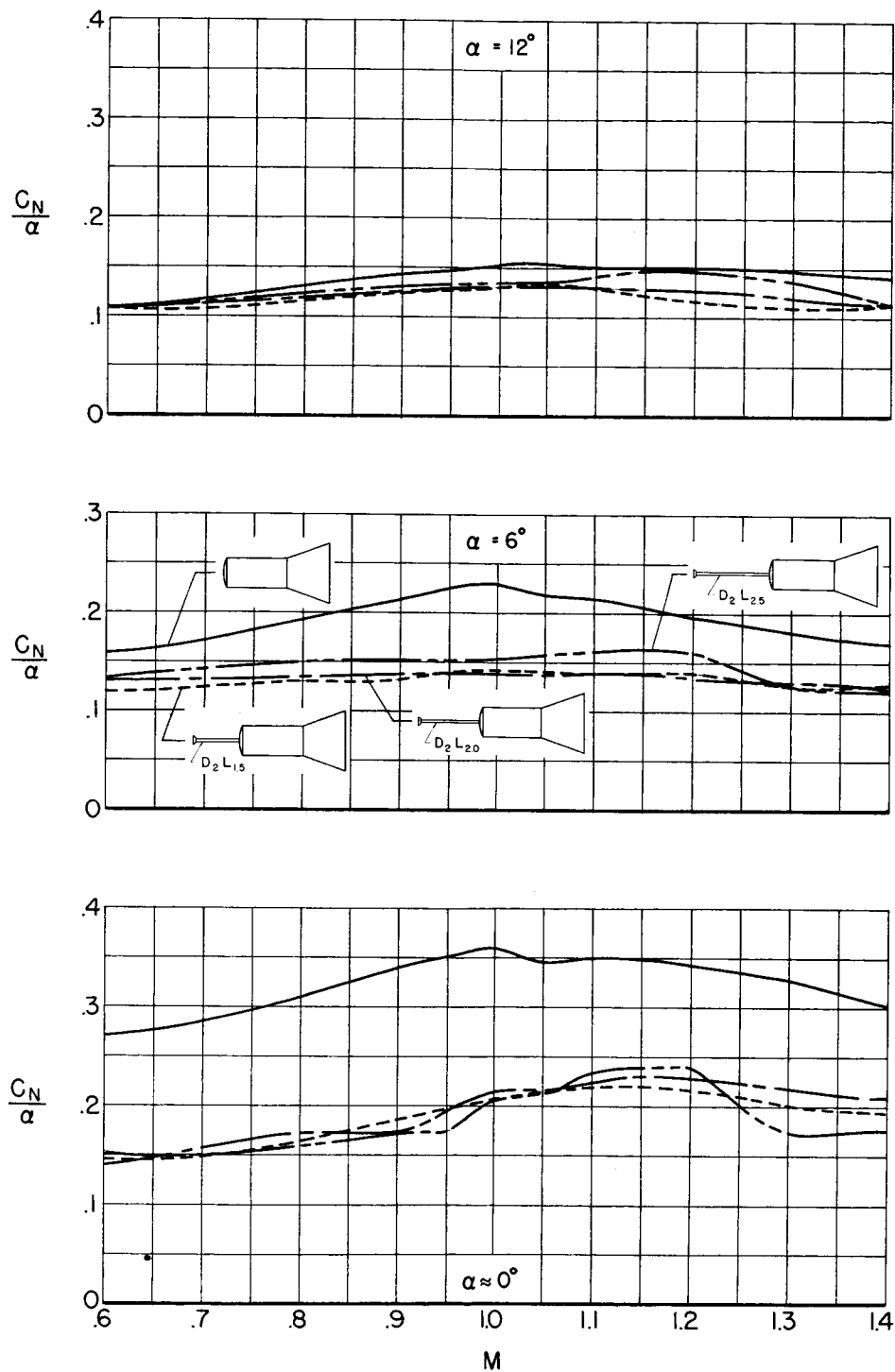


~~CONFIDENTIAL~~

(b) Flared models with hemispherical deflector.

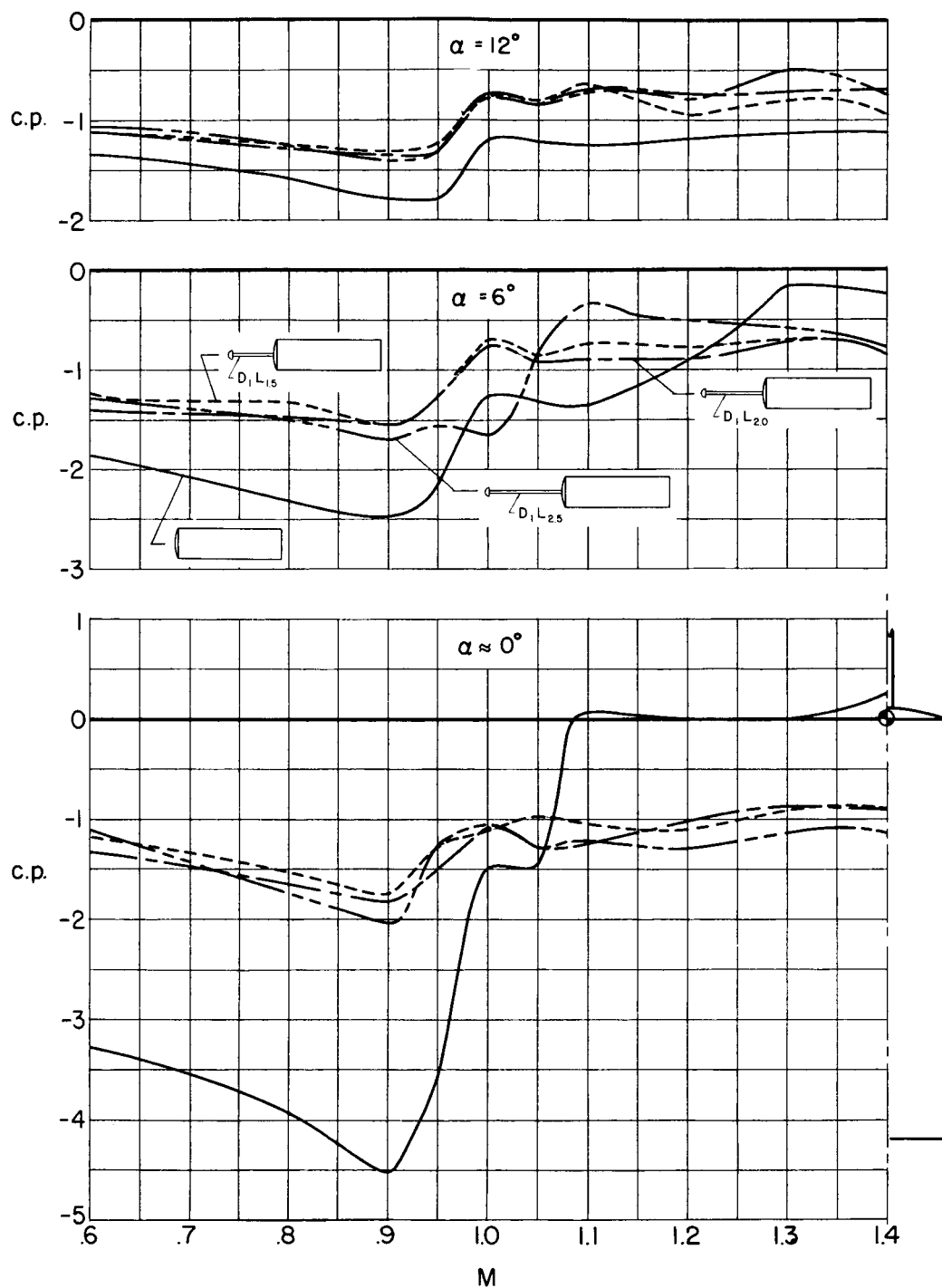
Figure 6.- Continued.

~~CONFIDENTIAL~~



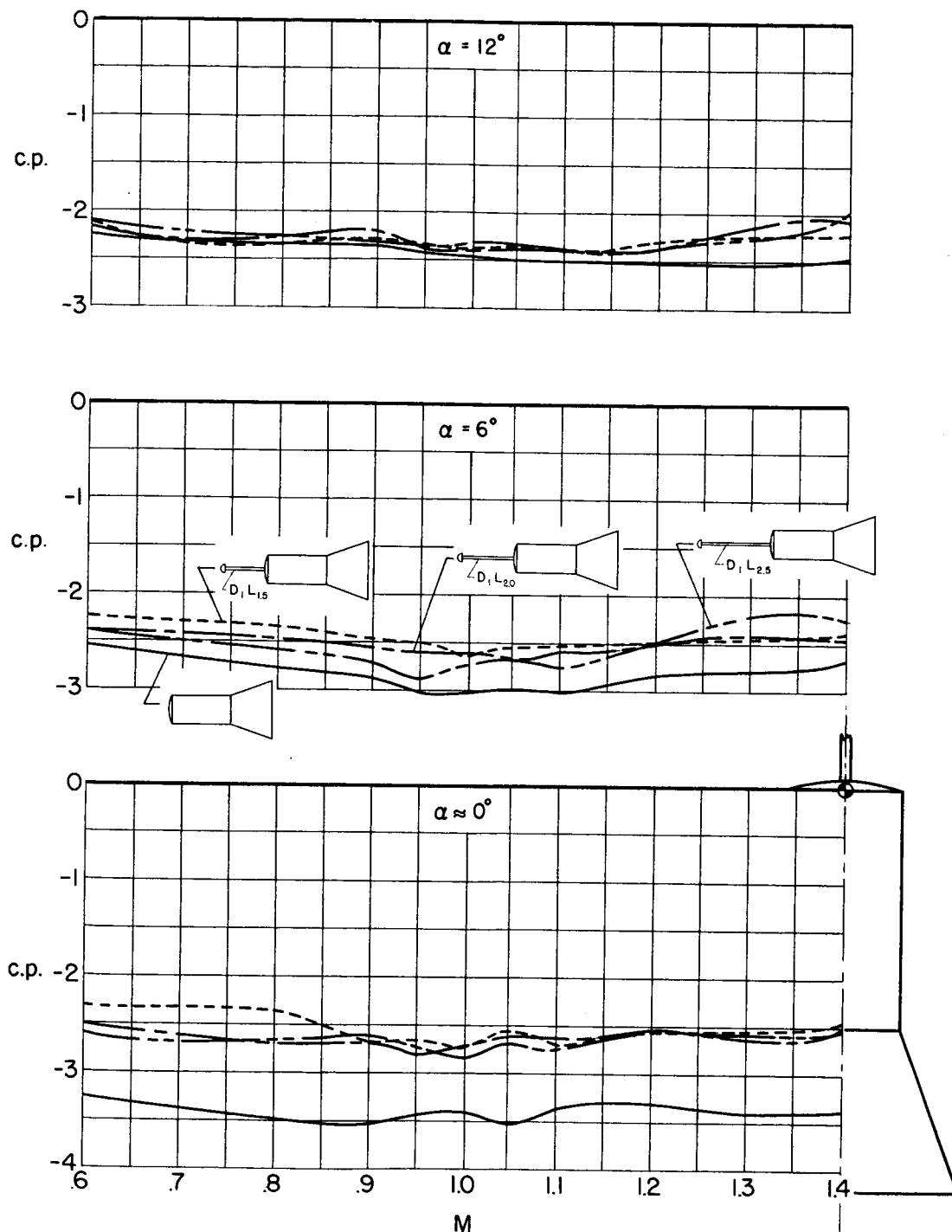
(c) Flared models with disk-shaped deflector.

Figure 6.- Concluded.



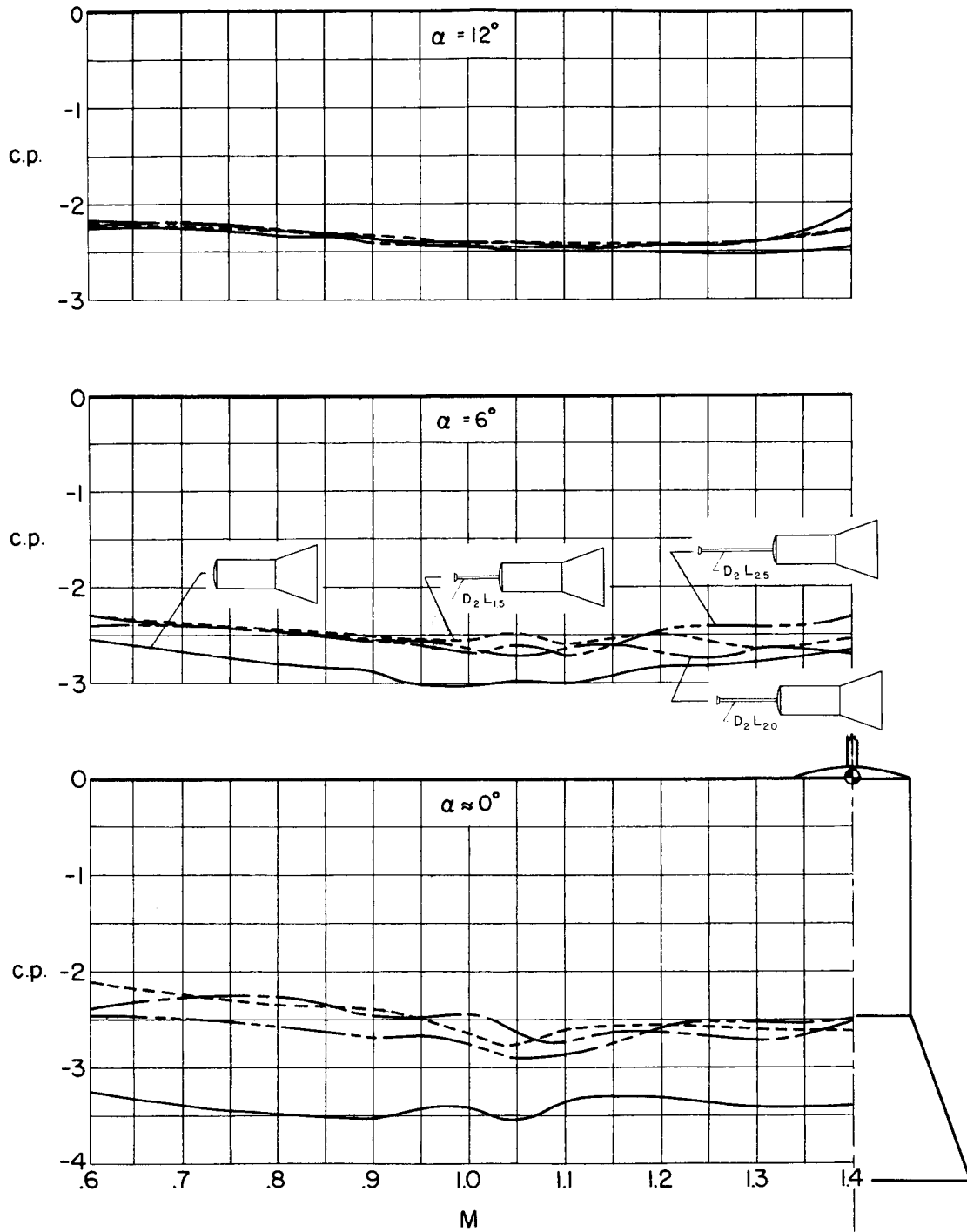
(a) Unflared models with hemispherical deflector.

Figure 7.- Effects of flow deflector length on the center-of-pressure location.



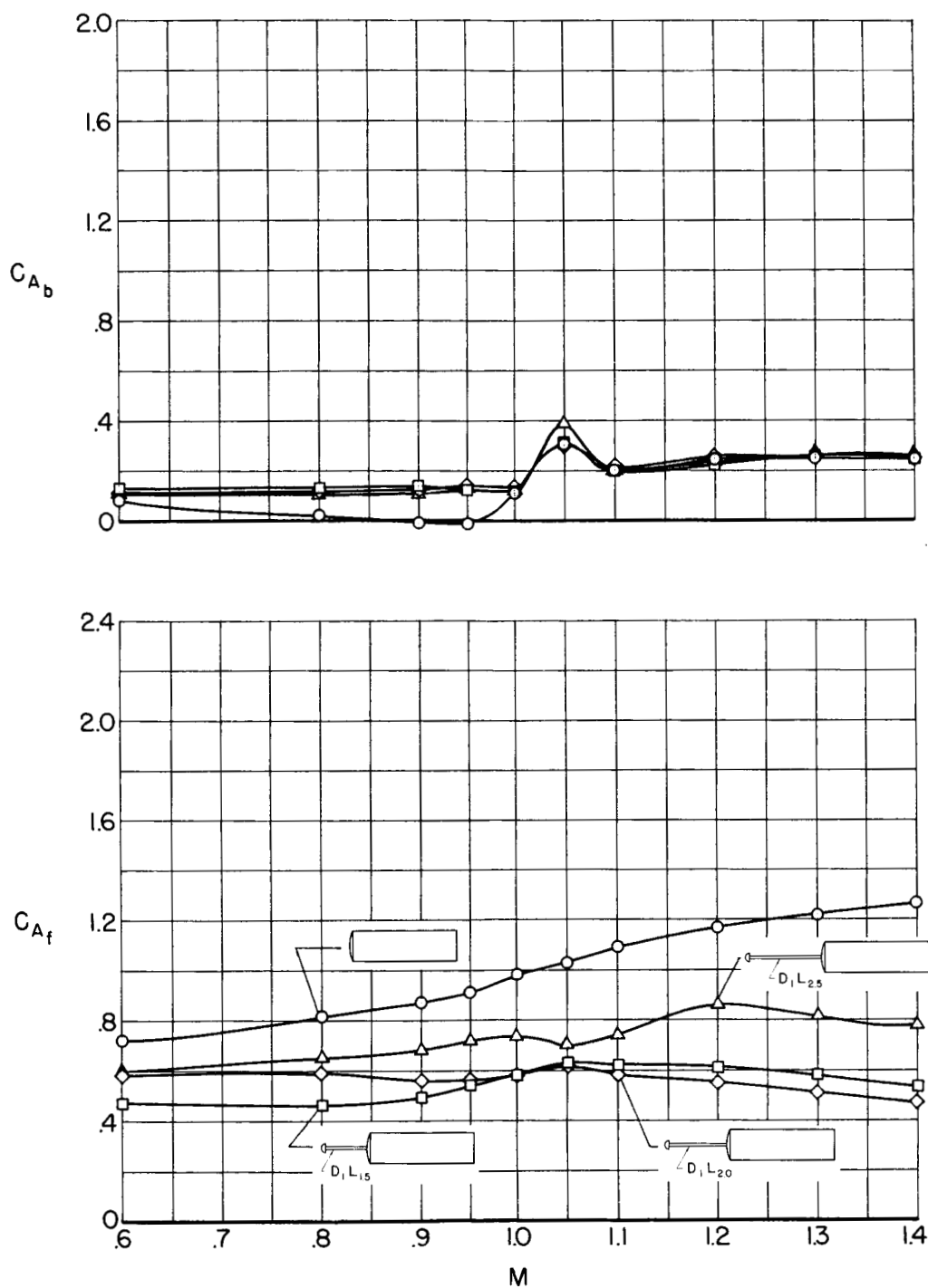
(b) Flared models with hemispherical deflector.

Figure 7.- Continued.



(c) Flared models with disk-shaped deflector.

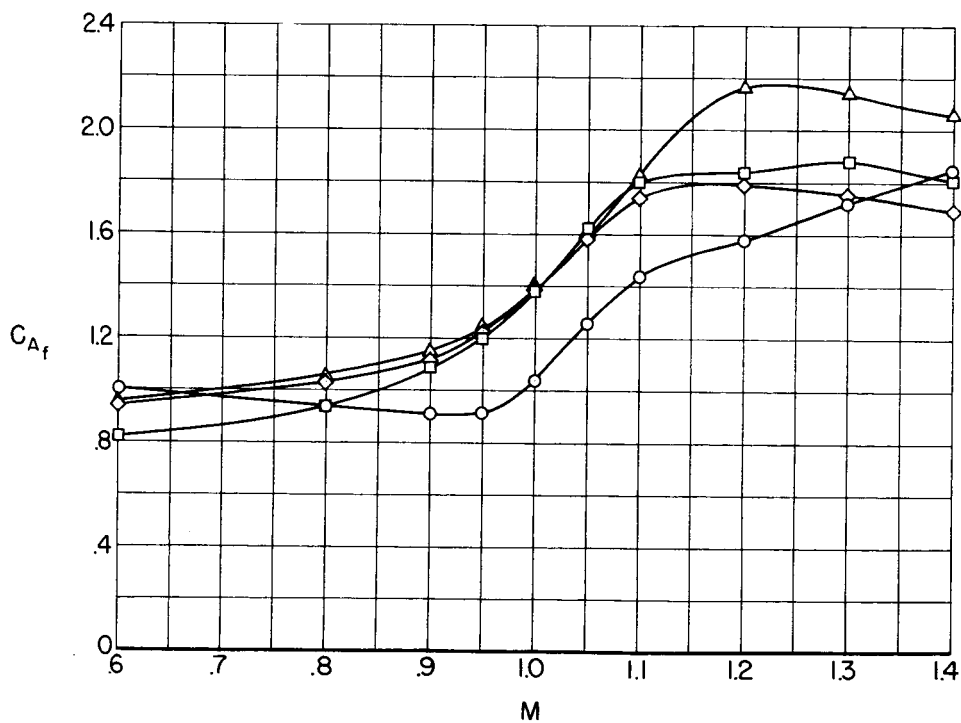
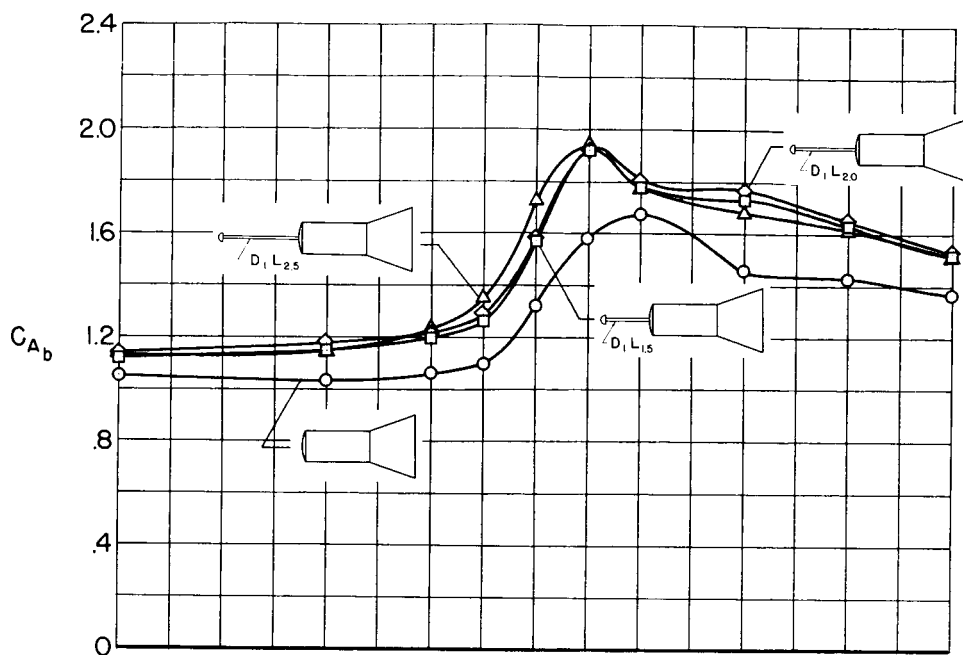
Figure 7.- Concluded.



(a) Unflared models with hemispherical deflector.

Figure 8.- Effects of flow deflector length on the forebody and base axial-force coefficients at  $0^\circ$  angle of attack.

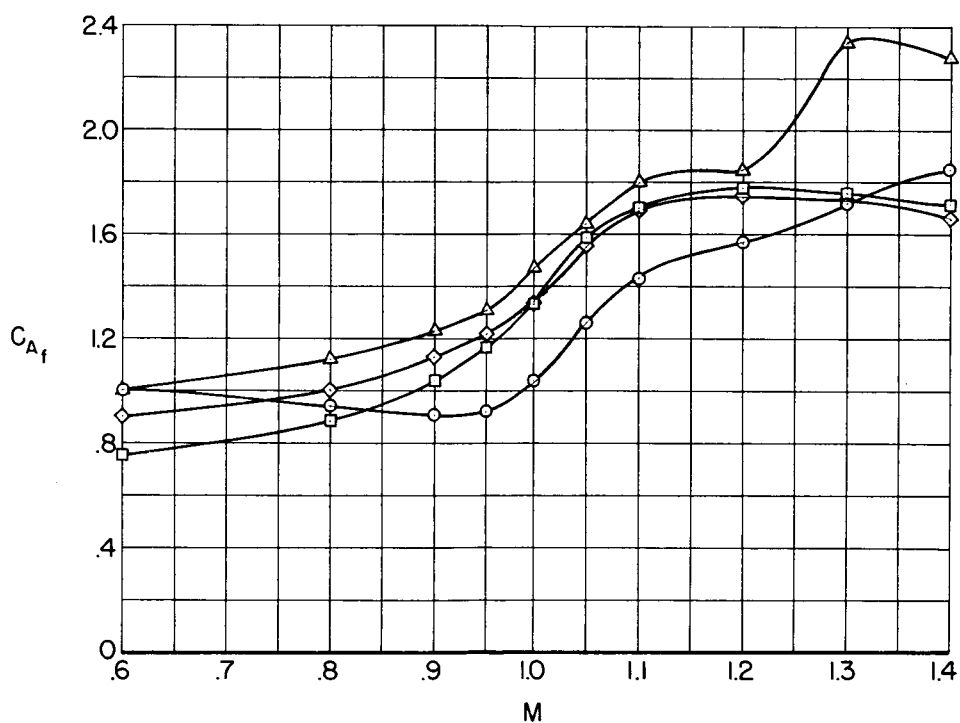
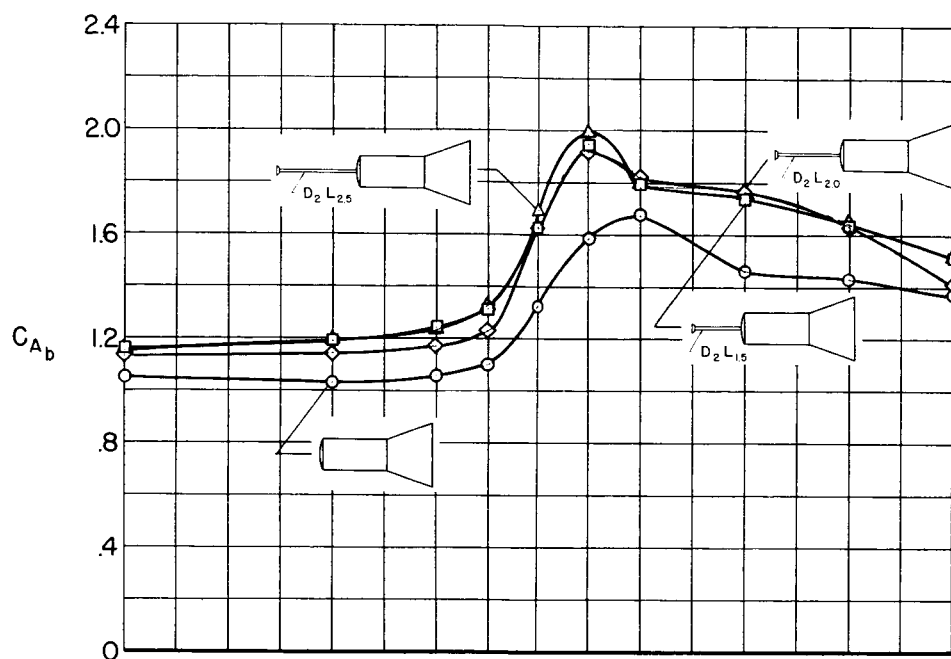
CONFIDENTIAL



(b) Flared models with hemispherical deflector.

Figure 8.- Continued.

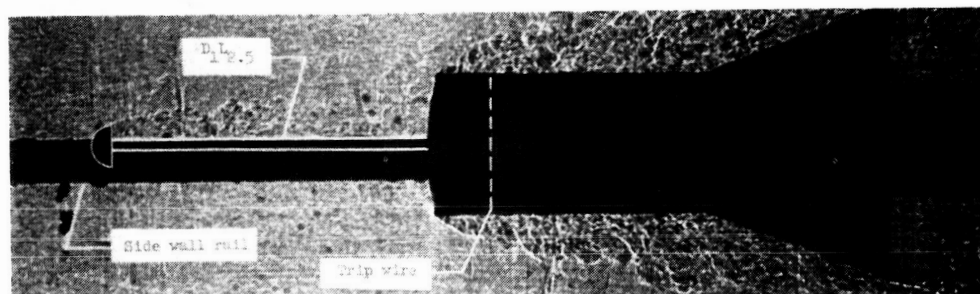
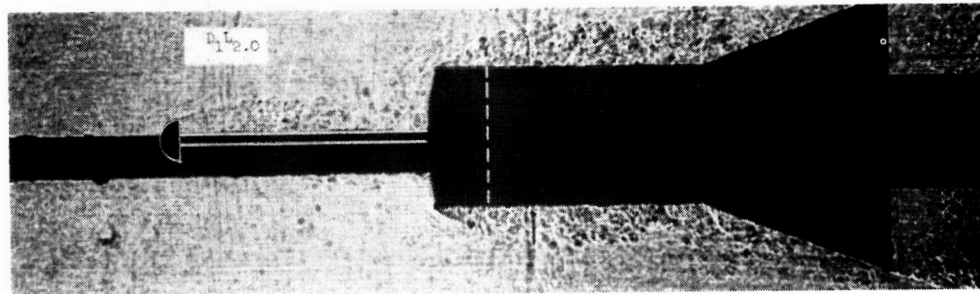
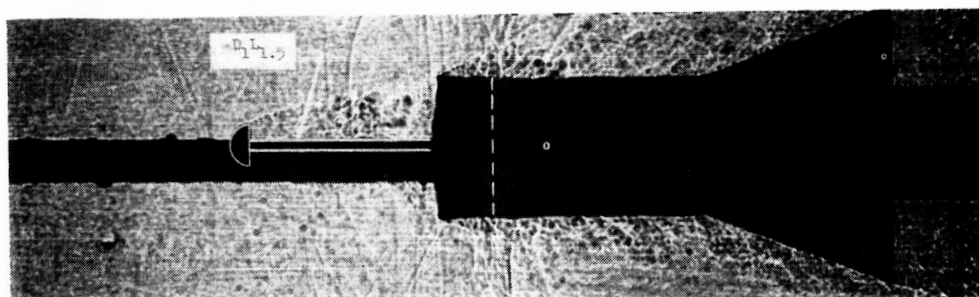
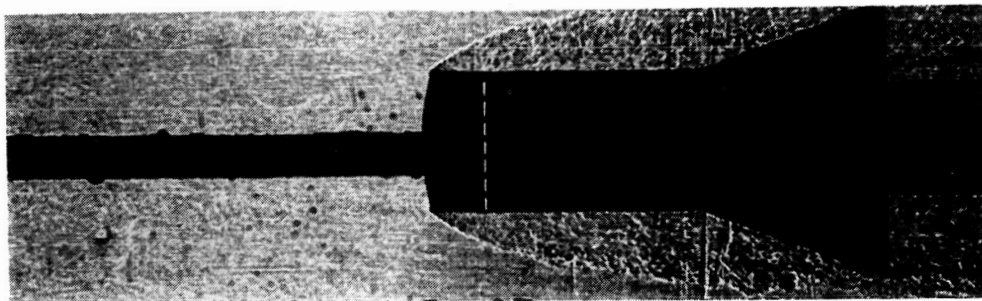
CONFIDENTIAL



(c) Flared models with disk-shaped deflector.

Figure 8.- Concluded.



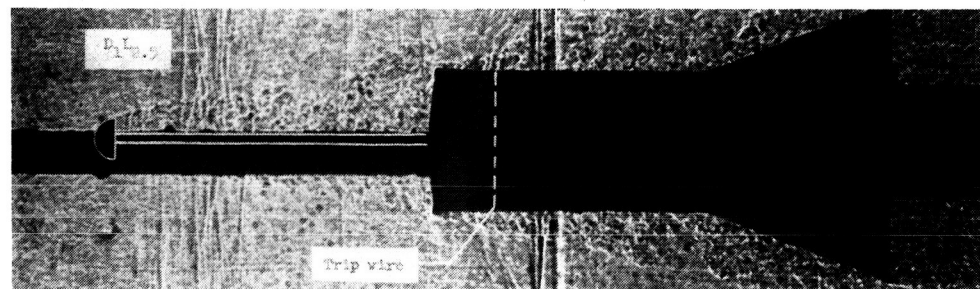
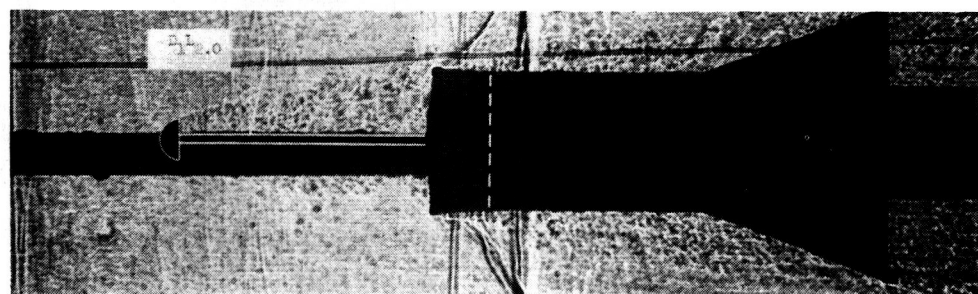
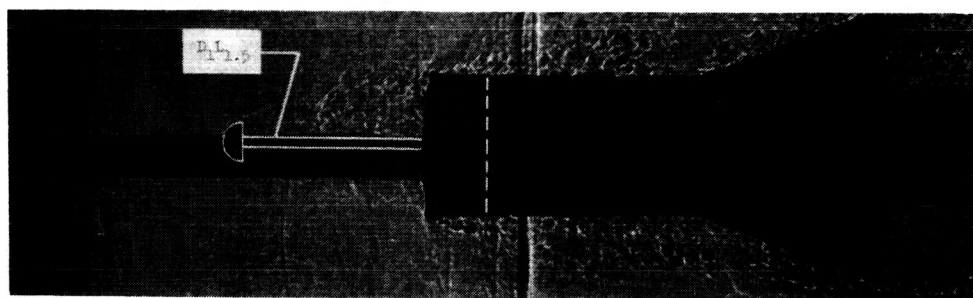
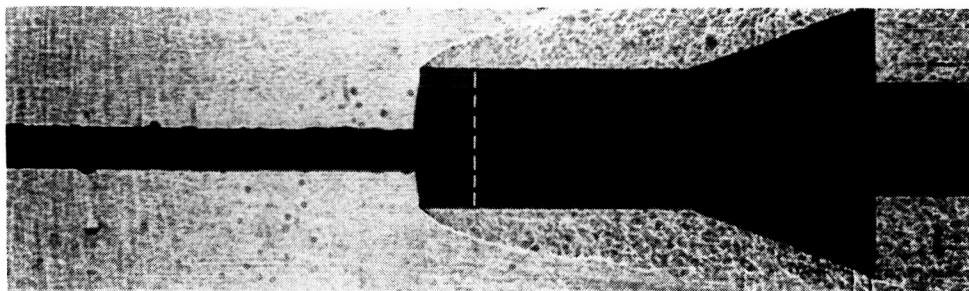


(a)  $M = 0.90$ .

Figure 9.- Effect of hemispherical flow deflectors on the flow patterns of the models with flared afterbodies at  $\alpha = 0^\circ$ .

~~CONFIDENTIAL~~

45



(b)  $M = 1.00$ .

Figure 9.- Continued.

~~CONFIDENTIAL~~

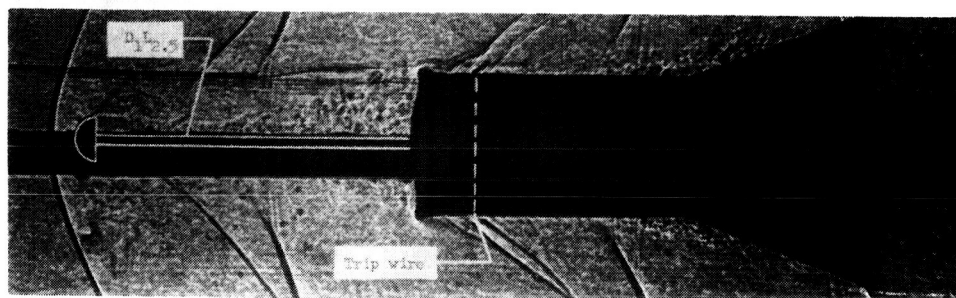
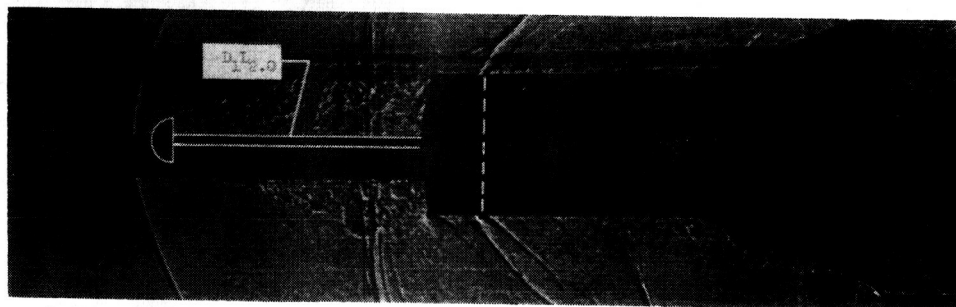
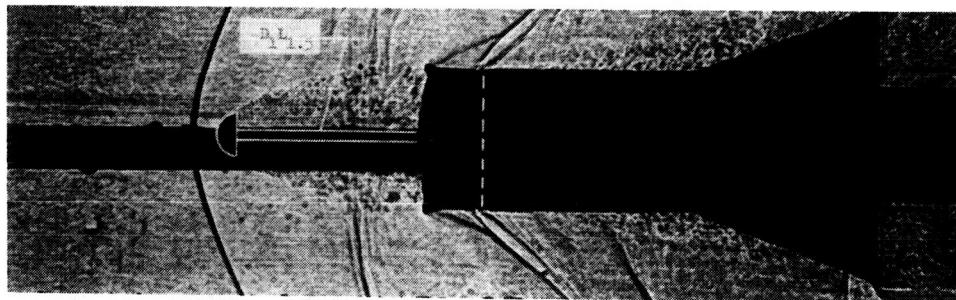
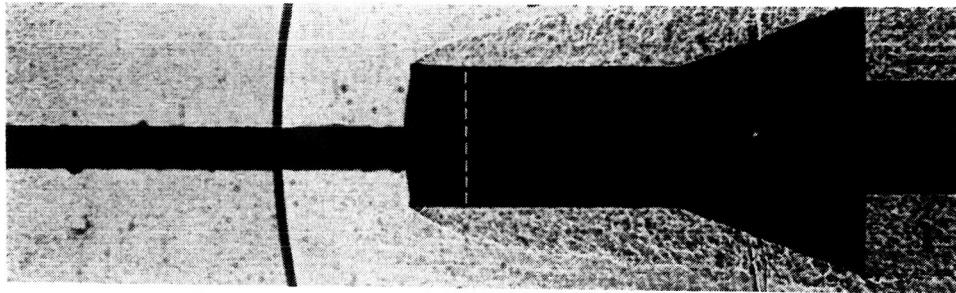
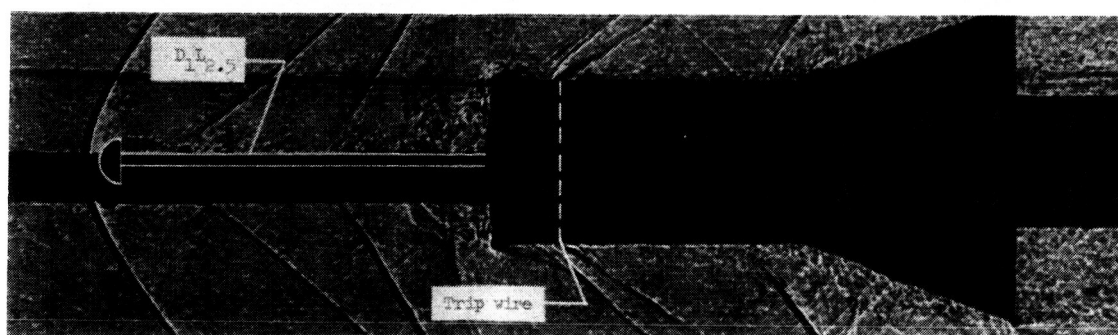
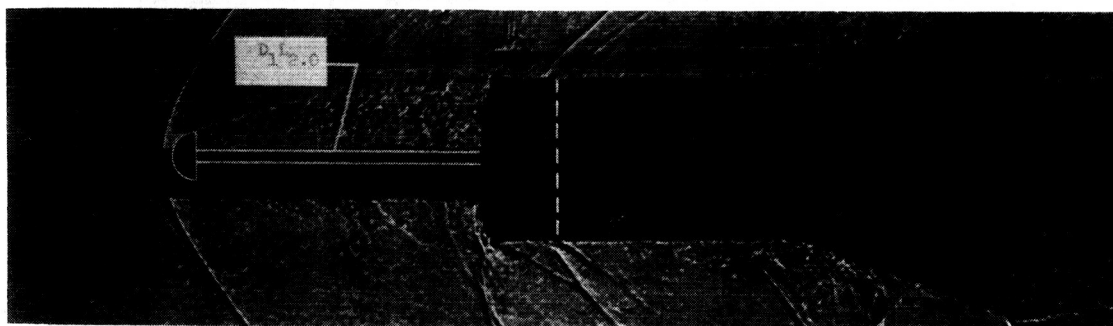
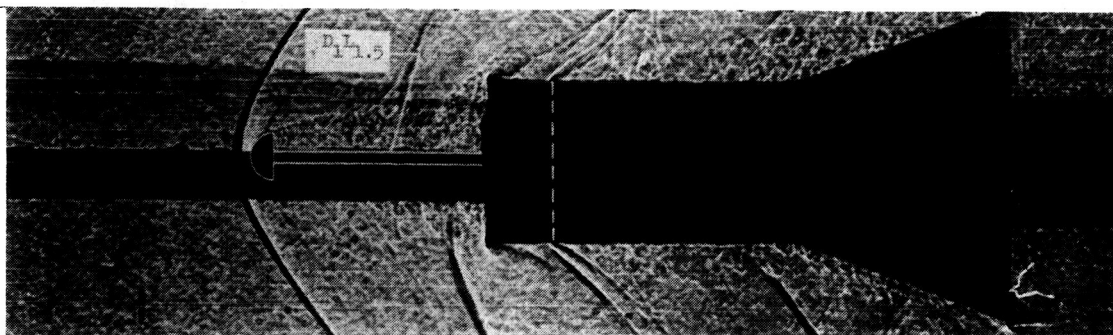
~~CONFIDENTIAL~~A  
4  
1  
0(c)  $M = 1.20$ .

Figure 9.- Continued.

~~CONFIDENTIAL~~



(d)  $M = 1.40$ .

Figure 9.- Concluded.

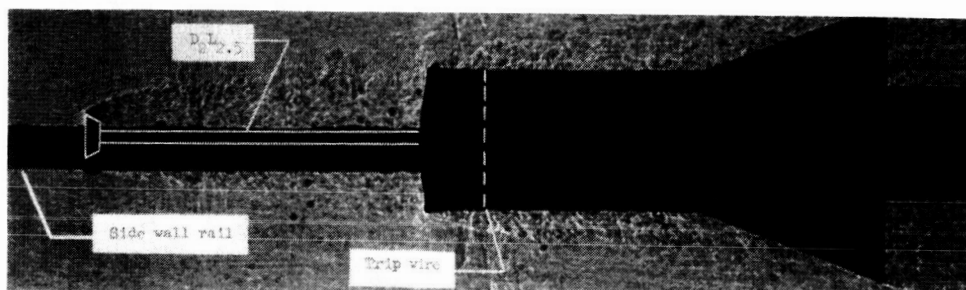
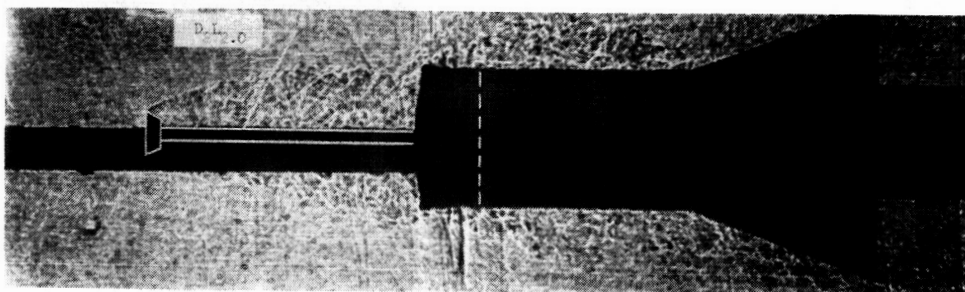
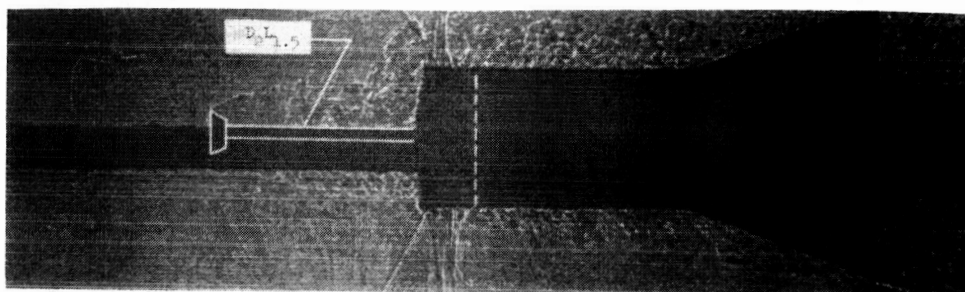
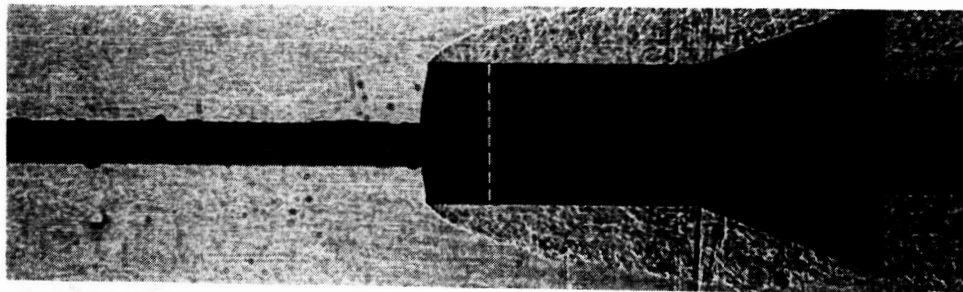
~~CONFIDENTIAL~~A  
4  
1  
0(a)  $M = 0.90$ .

Figure 10.- Effect of disk-shaped flow deflectors on the flow patterns of the models with flared afterbodies at  $\alpha = 0^\circ$ .

~~CONFIDENTIAL~~

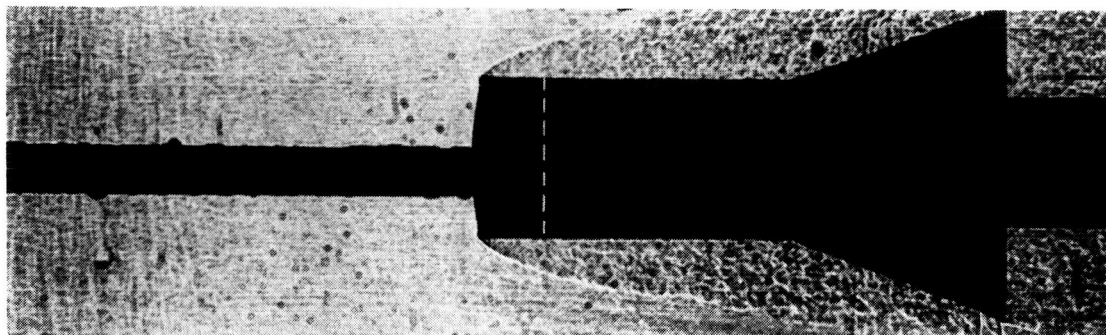
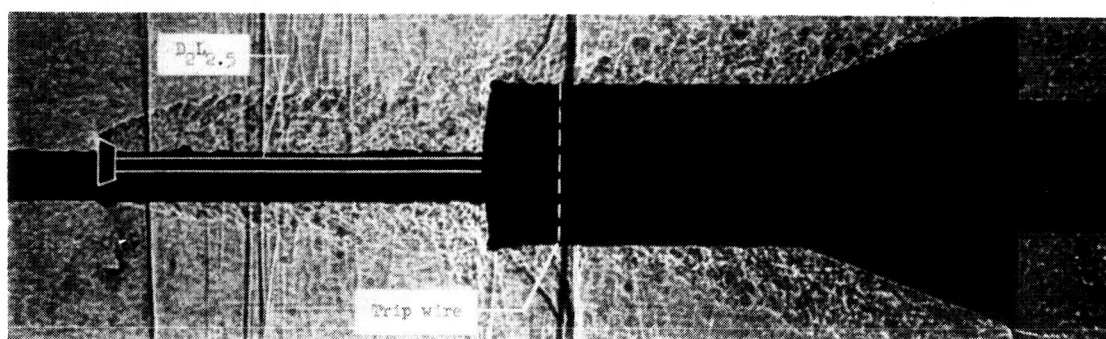
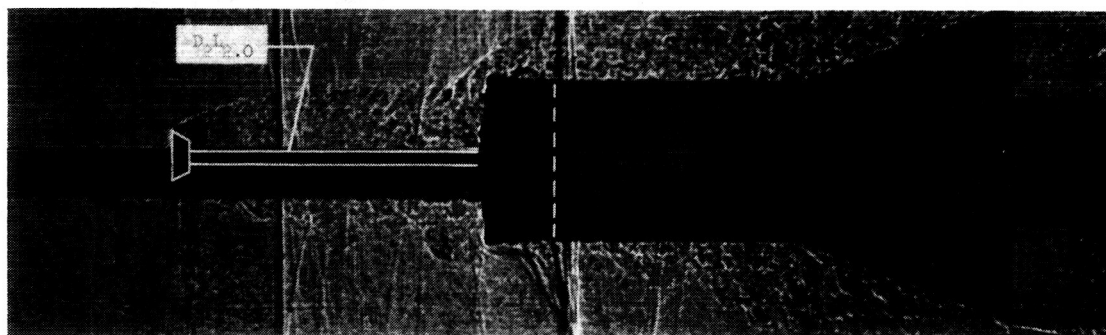
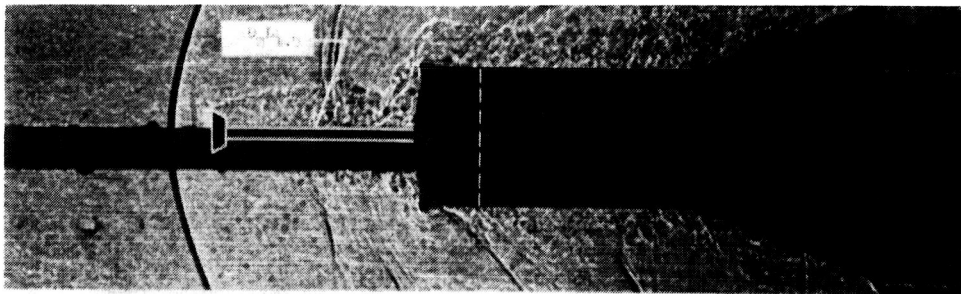
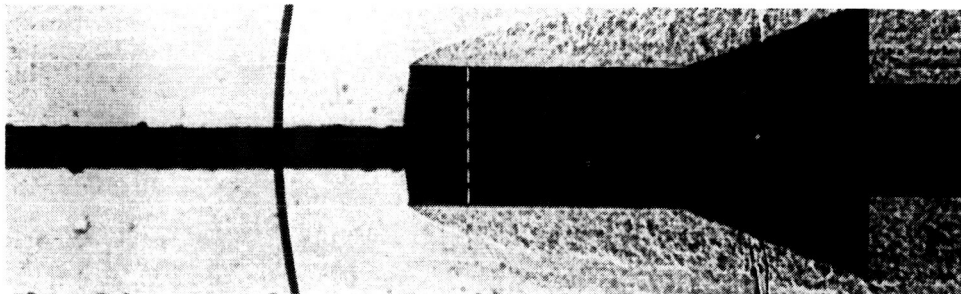
~~CONFIDENTIAL~~A  
4  
1  
0(b)  $M = 1.00$ .

Figure 10.- Continued.

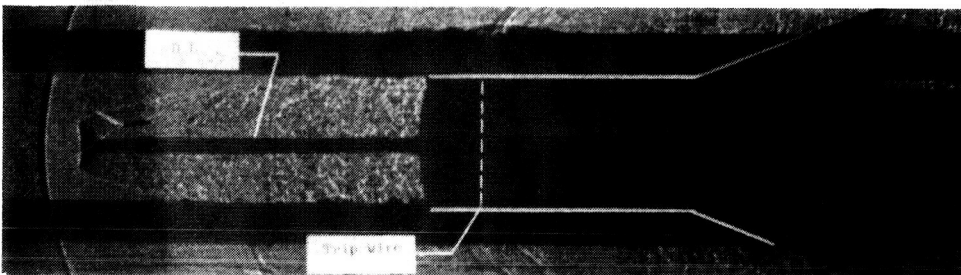
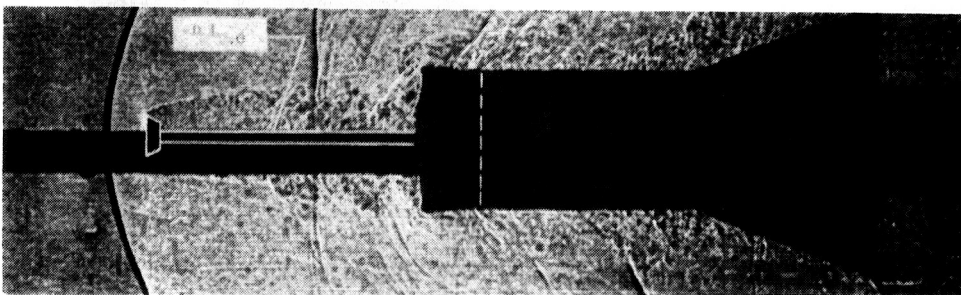
~~CONFIDENTIAL~~



[REDACTED]



A  
4  
1  
0

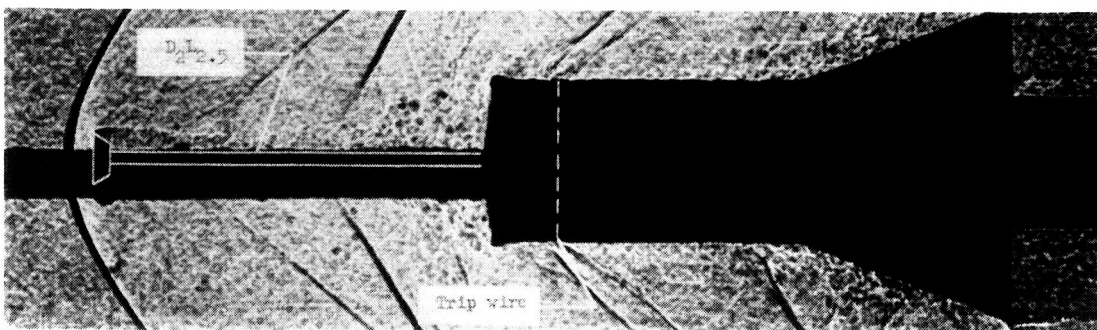
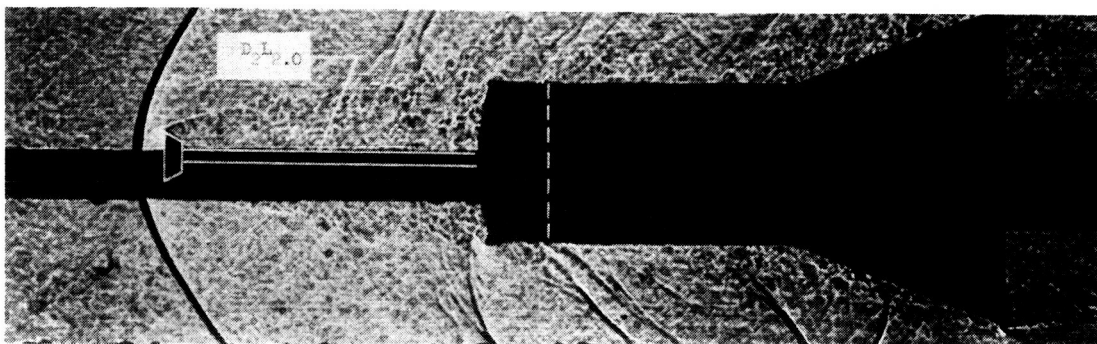
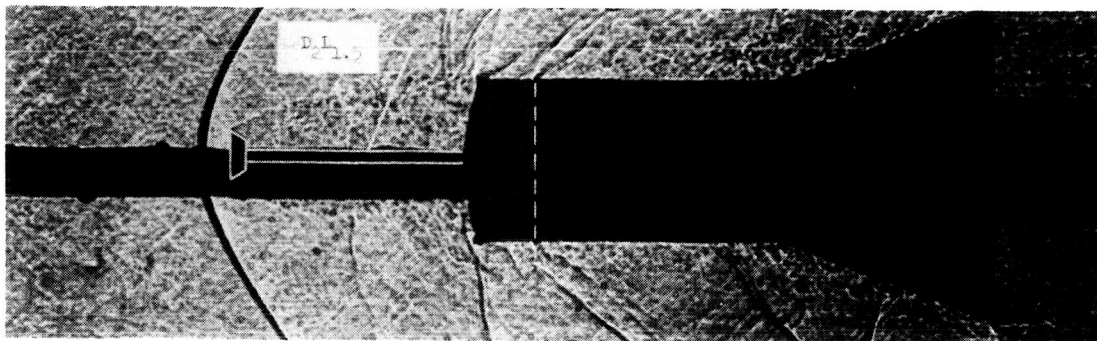


(c)  $M = 1.20$ .

Figure 10.- Continued.

[REDACTED]

~~CONFIDENTIAL~~



(d)  $M = 1.40$ .

Figure 10.- Concluded.

~~CONFIDENTIAL~~